



Perovskite oxide $\text{LaCr}_{0.25}\text{Fe}_{0.25}\text{Co}_{0.5}\text{O}_{3-\delta}$ as an efficient non-noble cathode for direct ammonia fuel cells

Georgina Jeerh^a, Peimiao Zou^a, Mengfei Zhang^a, Shanwen Tao^{a,b,*}

^a School of Engineering, University of Warwick, Coventry CV4 7AL, UK

^b Department of Chemical Engineering, Monash University, Clayton, Victoria 3800, Australia

ARTICLE INFO

Keywords:

Direct ammonia fuel cell (DAFC)
Perovskite
Oxygen reduction reaction (ORR)
Cathode
Rotating disk electrode (RDE)

ABSTRACT

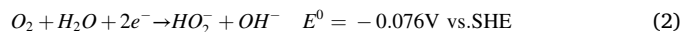
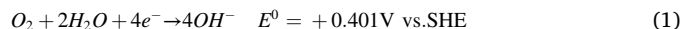
$\text{LaCoO}_{3-\delta}$ (LCO) based perovskites including $\text{LaCr}_{0.5}\text{Co}_{0.5}\text{O}_{3-\delta}$ (LCCO), $\text{LaFe}_{0.5}\text{Co}_{0.5}\text{O}_{3-\delta}$ (LFCO) and $\text{LaCr}_{0.25}\text{Fe}_{0.25}\text{Co}_{0.5}\text{O}_{3-\delta}$ (LCFCO) were prepared and their oxygen reduction reaction (ORR) activity was studied. The presence of both Cr and Fe played vital roles in enhancing activity, affecting structural and electronic properties respectively. Cr doping was associated with surface oxygen vacancy formation whilst Fe doping enhanced the onset and half-wave potential. Furthermore, the effects of calcinating temperatures were explored and LCFCO fired at 700 °C (LCFCO-700) gave superior activity. Remarkably, when LCFCO-700 was employed in a direct ammonia fuel cell (DAFC), an OCV of 0.72 V and a maximum current density of $\sim 320 \text{ mAcm}^{-2}$ was achieved when using air as the oxidant. Under similar conditions, DAFCs with $\text{LaCr}_{0.25}\text{Fe}_{0.25}\text{Co}_{0.5}\text{O}_{3-\delta}/\text{C}$ cathode, show comparable performance to the DAFC using Pt/C cathode, indicating that perovskite oxides, such as $\text{LaCr}_{0.25}\text{Fe}_{0.25}\text{Co}_{0.5}\text{O}_{3-\delta}$, are promising non-noble cathodes for DAFCs.

1. Introduction

A wide range of clean renewable energy resources are becoming growingly necessary to satisfy rising energy demands. Many of these, however, are intermittent in nature and rely heavily on external parameters such as wind and sun exposure [1]. It is therefore widely accepted that development of clean, reliable energy conversion and storage devices such as metal-air batteries, fuel cells and water splitting technologies will become progressively important in stabilising demand on the grid [2–19]. Commercial expansion of proton exchange membrane fuel cells (PEMFCs) and anion exchange membrane fuel cells (AEMFCs) however, are largely limited by the sluggish nature of the oxygen reduction reaction (ORR) and the high expense associated with Pt-based electrocatalysts [12,20–26]. For perspective, the current price of electrocatalysts account for greater than 30% of the total PEMFC cost [27–29]. On this basis, exploration of effective electrocatalysts to assist ORR at the lowest possible cost is essential for future use of these devices [12,21,30].

A spike in research interest towards AEMFCs has been prompted by the advantages of employing alkaline media over acidic. Amongst AEMFCs, direct ammonia fuel cells (DAFCs) have becoming increasingly popular due to the fuel's high energy density, large-scale global

production, extensive existing infrastructure, and low cost per unit energy [1,31–41]. These alkaline environments allow for faster ORR kinetics, the use of less corrosive conditions and use of cheaper non-platinum metal-group (non-PMG) electrocatalysts. This in turn enables a wider range of stable materials to be explored. Such non-PMG electrocatalysts often include carbon-transition metal hybrids, doped nanocarbons and perovskites [20–26]. The ORR pathway and rate determining steps in alkaline media are determined by the electrocatalyst and involves either a $4e^-$ or $2e^-$ pathway as shown in Eqs. (1) and (2) respectively [20,42]. The mechanistic factors governing ORR in alkaline media, however, are not widely understood and have proven to be rather complex [20,23,24,43].



Perovskite oxides have attracted much attention due to the vast flexibility in their chemical and electronic structure, allowing them to be easily exploited for the design of highly active and stable ORR electrocatalysts in alkaline media [12,13,20,21,23,24,29,42,44–51]. Such materials have the general formula ABO_3 and can accommodate a wide variety of cations in both the A and B sublattice [29]. Here, the A-site is

* Corresponding author at: School of Engineering, University of Warwick, Coventry CV4 7AL, UK.

E-mail address: s.tao.1@warwick.ac.uk (S. Tao).

<https://doi.org/10.1016/j.apcatb.2022.121919>

Received 19 June 2022; Received in revised form 13 August 2022; Accepted 27 August 2022

Available online 30 August 2022

0926-3373/© 2022 The Author(s). Published by Elsevier B.V. This is an open access article under the CC BY license (<http://creativecommons.org/licenses/by/4.0/>).

occupied by a rare earth metal (e.g. La, Gd, Pr or alkaline earth metal) usually with dodecahedral coordination, whilst the B-site is generally a transition metal (e.g. Mn, Cr, Fe, Ni, Co) that resides in corner-sharing octahedra [29,52]. It is widely accepted that optimum ORR activity for perovskites follow Sabatier's principle of catalysis, whereby the interaction between the catalyst and the surface adsorbed oxygen species is moderate [53]. Unfortunately, it is challenging to directly measure the adsorbate binding energy at the surface. Focus has therefore been shifted towards identifying activity descriptors which can be linked to adsorbate binding energy and govern activity [54–56]. By using molecular orbital theory, Suntivich et al. established a volcano-type relationship between intrinsic ORR activity and the σ^* orbital (e_g) occupation of B-site ions. It was found that perovskites with near unity e_g orbital occupancy such as LaMnO_3 ($t_{2g}^3e_g^1$), LaCoO_3 ($t_{2g}^5e_g^1$) and LaNiO_3 ($t_{2g}^6e_g^1$), exhibit optimum ORR activity [23,57]. In cases where there was a lack of e_g filling such as in LaCrO_3 ($t_{2g}^3e_g^0$), the B- O_2 bonding was too strong and resulted in the O_2^-/OH^- exchange becoming the rate determining step. Alternatively, where there was too much e_g filling such as in LaFeO_3 ($t_{2g}^3e_g^2$),

²), the interaction was too weak and the regeneration of OH^- ions was the rate determining step. As well as e_g orbital filling and metal-oxygen covalency, positioning of the d-band centre, oxidation states and oxygen vacancies have also been reported to affect ORR activity and should not be considered independently [21,58–60].

More recently, strategically doping into the B-site and varying elemental composition has proven to be a promising strategy to design highly active perovskite catalysts for ORR. Sunarso et al. compared ORR activity of LaMO_3/C and $\text{LaNi}_{0.5}\text{M}_{0.5}\text{O}_{3-\delta}/\text{C}$ ($\text{M} = \text{Ni, Co, Fe, Mn and Cr}$) electrocatalysts in 0.1 M KOH. It was reported that LaCoO_3 and $\text{LaNi}_{0.5}\text{Mn}_{0.5}\text{O}_{3-\delta}/\text{C}$ were the most active amongst the series tested [47]. Sun et al. investigated the structure property relationships between B-site metal substitution in $\text{LaMn}_x\text{Co}_{1-x}\text{O}_3$ ($x = 0, 0.25, 0.3, 0.35, 0.5, 1$) and the electrochemical performance. The optimised $\text{LaMn}_{0.3}\text{Co}_{0.7}\text{O}_3$ perovskite demonstrated an enhanced half-wave potential of 0.72 V compared to that of LaCoO_3 (0.668 V) in 0.1 M KOH [48]. Wang et al. reported that structural and compositional characterisation revealed that $\text{La}_{0.8}\text{Sr}_{0.2}\text{Mn}_{1-x}\text{Ni}_x\text{O}_{3-\delta}$ ($x = 0.2$ and 0.4) contained more oxygen vacancies than undoped $\text{La}_{0.8}\text{Sr}_{0.2}\text{MnO}_3$ as well as a certain amount of Ni^{3+} ($e_g = 1$) on the surface. This allowed for $\text{La}_{0.8}\text{Sr}_{0.2}\text{Mn}_{0.6}\text{Ni}_{0.4}\text{O}_{3-\delta}$ to exhibit activity similar to that of commercial Pt/C at a reduced cost, making it an efficient cathodic electrocatalyst for Li-air batteries [49].

Despite the significant body of work described above, certain parameters affecting the electrocatalytic performance of LaCoO_3 towards ORR, such as the effects of doubly doping at the B-site, have not been as widely explored. In the present work, a series of B-site substituted $\text{LaCoO}_{3-\delta}$ (LCO) perovskites, including $\text{LaCr}_{0.5}\text{Co}_{0.5}\text{O}_{3-\delta}$ (LCCO), $\text{LaFe}_{0.5}\text{Co}_{0.5}\text{O}_{3-\delta}$ (LFCO) and $\text{LaCr}_{0.25}\text{Fe}_{0.25}\text{Co}_{0.5}\text{O}_{3-\delta}$ (LCFCO), were synthesised via a conventional combustion method and mixed with carbon black to investigate their activity towards ORR in O_2 -saturated 0.1 M KOH solution using a rotating disk electrode (RDE) technique. Thorough investigation into the structure property relationship of the electrocatalysts was conducted to study the synergetic effects of doping both Fe- and Cr at the B-site of LCO. To the best of our knowledge, this is the first report on the effects of strategically introducing two dopants into the Co B-site of LCO on oxygen reduction activity and to truly exploit the flexible nature of perovskite oxides. The effects of firing temperature of LCFCO on its electrochemical properties was also investigated. Finally, applicability of the perovskite cathode in a direct ammonia fuel cell was explored to assess the potential of the catalyst in a practical device as well as its ability to compete with expensive platinum group metals (PGMs). It was found DAFCs with $\text{LaCr}_{0.25}\text{Fe}_{0.25}\text{Co}_{0.5}\text{O}_{3-\delta}/\text{C}$ cathode exhibits comparable performance to those with Pt/C cathode.

2. Experimental

2.1. Materials

$\text{La}(\text{NO}_3)_3 \cdot 6\text{H}_2\text{O}$ (99.9%, Sigma Aldrich), $\text{Co}(\text{NO}_3)_2 \cdot 6\text{H}_2\text{O}$ ($\geq 98\%$, Sigma Aldrich), $\text{Cr}(\text{NO}_3)_3 \cdot 9\text{H}_2\text{O}$ ($\geq 98\%$, Sigma Aldrich) and $\text{Fe}(\text{NO}_3)_3 \cdot 9\text{H}_2\text{O}$ ($\geq 98\%$, Sigma Aldrich) were used as metal precursors with no further purification. Citric acid (99 +%, Alfa Aesar) and ethylene glycol (Fisher Scientific) were used during the synthesis process. Carbon black (Vulcan XC-72) and Nafion solution (5 wt%, Sigma Aldrich) were added to prepare an ink for the RDE tests. Pt/C was commercially purchased (commercial 20 wt% platinum on carbon black, Alfa Aesar). Carbon cloth (Toray, wet proofing 1–5%) was used as the diffusion substrate layer for fuel cell tests along with a PiperION-A20-HCO₃ TP-85 alkaline membrane (Versogen, 20 μm) and PiperION BP-100 ionomer (Versogen). Other chemicals such as isopropanol and KOH were all analytical reagents purchased from Alfa Aesar.

2.2. Synthesis of perovskite powders

The perovskite powders were synthesised using a conventional combustion method [61]. In brief, appropriate amounts of the metal nitrate precursors were dissolved in an aqueous solution at room temperature. Citric acid was added in a molar ratio of 1:1.2:1.2 of total metal ions: citric acid:ethylene glycol. The resulting solution was stirred and heated to 120 °C. After the evaporation of water, the sample was heated to 410 °C to form an ash which was finely ground using an agate mortar and pestle. The powder was calcinated in air at 500 °C for 2 h with a heating/cooling rate of 5 °Cmin⁻¹ before being reground and further calcinated at 1000 °C for 4 h with a heating/cooling rate of 3 °Cmin⁻¹ to obtain the final perovskite phase. The collected $\text{LaCoO}_{3-\delta}$, $\text{LaCr}_{0.5}\text{Co}_{0.5}\text{O}_{3-\delta}$, $\text{LaFe}_{0.5}\text{Co}_{0.5}\text{O}_{3-\delta}$ and $\text{LaCr}_{0.25}\text{Fe}_{0.25}\text{Co}_{0.5}\text{O}_{3-\delta}$ samples were labelled LCO, LCCO, LFCO and LCFCO respectively. The synthesis of LCFCO was further explored by adjusting the final calcinating temperature to 600, 700, 800 and 900 °C, labelled as LCFCO-600, LCFCO-700, LCFCO-800 and LCFCO-900 respectively.

2.3. Physicochemical characterisation

X-ray Powder Diffraction (XRD) analysis was used to examine the phase and purity of the perovskite powders. Measurements were carried out at room temperature on a PANalytical X'Pert Pro diffractometer (Cu K α source, 1.5405 Å) and collected in the 2θ range of 20–80° with a step of 0.0167°. Phase analysis and identification was conducted via the HighScore software. It should be noted that particle size can affect intrinsic ORR activity, therefore, to gain insight into size-activity relationship, crystallite sizes were calculated by the Scherrer equation using data extracted from the XRD patterns (Eq. S(1–3)).

The above methods give an average value of crystalline sizes; however, real samples usually consist of grains with different domains. To evaluate the distribution of grain sizes and account for the non-coherent domains, Scanning Electron Microscopy (SEM) images were taken. SEM was used to examine the morphology of the catalyst at the surface using a Zeiss SUPRA 55-VP, equipped with an Energy-Dispersive X-ray (EDS) spectrometer for elemental analysis. Specimens were prepared prior to testing by depositing small amounts of the powder and coated with Au. Raman spectroscopy was conducted using a Renishaw InVia Raman Microscope with an exciting wavelength of 532 nm.

X-ray Photoelectron Spectroscopy (XPS) analysis was measured using a monochromated Al K α X-ray source on a Kratos Axis Ultra DLD spectrometer (Kratos Analytical, Manchester, UK). The data was collected at a take-off angle of 90° to the surface plane and analysed using the Casa XPS package. To prevent the surfaces becoming positively charged, charge neutralization was employed and the spectra were later referenced to the C-C peak at 285.0 eV during analysis.

Textural properties were assessed via N_2 adsorption-desorption

isotherms of the perovskite powders recorded at liquid N₂ temperature using a Micromeritics ASAP 2020 apparatus. Samples were degassed at 300 °C for 1 h. Specific surface areas (SSA) were determined by applying Brunauer-Emmett-Teller (BET) method.

2.4. Electrochemical characterisation

The electrochemical activity of the samples towards ORR were measured via a rotating disk electrode (RDE) technique in O₂-saturated 0.1 M KOH solution at room temperature (ca. 20 °C). An ink was prepared by mixing of the perovskite catalyst powder and carbon black (Vulcan XC-72R) in a 5:1 mass ratio respectively. The oxide was physically mixed with high surface area carbon black (Vulcan XC-72R, specific surface area 216 m²g⁻¹).

to facilitate electrical contact between the oxide particles and help eliminate issues relating to electronic conductivity, favouring complete utilisation of the perovskite surface [62]. The resulting powders were dispersed and sonicated in ethanol and Nafion solution (binding agent) before being pipetted onto a glassy carbon (GC) disk electrode (PINE research, AFE2M050GC) and dried at room temperature to form a thin film. The geometric surface area of the GC electrode was 0.196 cm². The catalyst coated GC electrode was mounted onto a RDE shaft (AFE6MB) attached to a modulated speed regulator (PINE research, MSR) and used as the working electrode in a typical three-electrode set up contained in an electrochemical cell kit (PINE research, AKCELL2). Pt mesh and Ag/AgCl (saturated KCl) were used as the counter and reference electrodes respectively.

To assess ORR activity, electrochemical characterization was determined by recording polarisation curves on a Solartron 1470E multi-channel cell test system. Tests were conducted in O₂-saturated 0.1 M KOH solution using the potential range of −0.6–0.1 V vs. Ag/AgCl (0.36–1.06 V RHE) at a scan rate of 10 mVs⁻¹ and various rotation rates (100, 400, 900, 1600 rpm) of the RDE. Chronopotentiometry tests were conducted in 0.1 M KOH at room temperature under a fixed potential of −0.4 V vs. Ag/AgCl. From analysis of the ORR polarisation curves, Koutecky-Levich (K-L) plots were exploited to calculate the electron transfer number for all electrocatalysts using the following equations [42,63]:

$$\frac{1}{I} = \frac{1}{I_L} + \frac{1}{I_k} = \frac{1}{B\omega^{1/2}} + \frac{1}{I_k} \quad (3)$$

$$B = 0.62nFC_0D_0^{2/3}V^{-1/6} \quad (4)$$

where I is the measured current density, I_k and I_L are the kinetic and limiting current density respectively, ω is the angular velocity of the disk, n is the electron transfer number, F is the Faraday constant (96485 C mol⁻¹), C_0 is the bulk concentration of O₂ (1.2 × 10⁻⁶ mol cm⁻³), D_0 is the diffusion coefficient of O₂ in 0.1 M KOH (1.9 × 10⁻⁵ cm² s⁻¹), and V is the kinematic viscosity of the electrolyte (0.01 cm² s⁻¹).

2.5. Electrode preparation

Carbon cloth was washed and sonicated in dilute hydrochloric acid, isopropanol and deionized water. The cathode was prepared by coating the perovskite catalyst onto the pre-treated carbon cloth with a loading of 3.4 mg_{oxide}cm⁻². The perovskite powder was physically mixed with high surface area carbon black (Vulcan XC-72R) in a weight ratio of 1:1 to facilitate electrical contact between the oxide particles and help eliminate issues relating to electronic conductivity, favouring complete utilisation of the perovskite surface [62]. Utilising propanol as the solvent, the PiperION TP-100 ionomer was ultra-sonicated in an ice-water bath for 1 h with perovskite/C (perovskite/C:PiperION = 4:1 wt ratio) and PTFE (10 wt%) to form a uniform dispersion. The ink was then brushed onto the carbon cloth and left to dry. The loading of the electrode was 1.23 mg_{oxide}cm⁻². For comparison, a similar method was

employed to fabricate a Pt/C electrode with a loading of 0.4 mg_{PGM}cm⁻². PtIr(40 wt%)/C(60 wt%) powder was prepared using a method described elsewhere [64]. Utilising propanol and water as the solvent, the PiperION TP-100 ionomer was ultra-sonicated in an ice-water bath for 1 h with PtIr/C (PtIr/C:PiperION = 4:1 wt ratio) to form a uniform dispersion. The ink was then brushed onto the pre-treated carbon cloth and a loading of 2.2 mg_{PGM}cm⁻² was obtained.

2.6. Single-cell evaluation test

The test conditions for the single cell with an active area of 1 cm² was anode fuel: 2 mLmin⁻¹ 7 M NH₃H₂O at 3 bar and cathode fuel: 180 mLmin⁻¹ CO₂-free air fed through a humidifier at a temperature of 95 °C at 2 bar. The cell temperature was 80 and 100 °C and the corresponding polarisation curves were obtained using a Solartron 1287 A Electrochemical Station. The stability of the ammonia fuel cell was tested at fixed current density of 50 mA cm⁻² at an operating temperature of 100 °C. The anodic backpressure was held at 3 bar whilst the cathodic backpressure was held at 2 bar.

3. Results and discussion

3.1. Sample characterisation

The room temperature XRD patterns of the parent LCO sample as well as the singly and doubly doped counterparts are compared in Fig. 1b. Detailed lattice parameters are listed in Table 1. The XRD analysis reveals that the intense reflections of the LCO perovskite were well indexed to the rhombohedral crystal system (PDF 00-048-0123) and agrees well with literature [65,66]. The perovskite phase is successfully formed for all samples with no indications of any structural or phase changes, demonstrating that Cr and Fe are successfully introduced into the B-site.

There is a clear gradual shift in diffraction peaks to lower 2θ values on doping of Cr and/or Fe which indicates expansion of the unit cell. On introduction of Cr into the B-site of the LCO perovskite, the peaks shift to lower 2θ angles with respect to the parent structure. This can be seen with the (100) peak highlighted in Fig. 1b (right). This shift can be attributed to the larger crystal radius of Cr³⁺ (0.755 Å), compared to intermediate-spin (IS) Co³⁺ ions, which is presumed to be between that of low-spin (LS) (0.685 Å) and HS (0.750 Å) Co³⁺ when the coordination number is 6 [42,67–69]. On substitution of the B-site with Fe, there is a further obvious shift in diffraction peaks towards lower 2θ angles. This can be owed to the larger crystal radius of high-spin (HS) Fe³⁺ ions (0.785 Å) compared to that of both Cr³⁺ and Co³⁺, henceforth a greater expansion of the lattice can be expected to accommodate for the larger crystal radius [42,67–69]. Ivanova et al. reported similar results showing lattice expansion when Fe was introduced into LaCo_{1-x}Fe_xO₃ due to the larger ionic radius of high spin Fe³⁺ ions [70]. Moreover, when the B-site is dual substituted with both Cr and Fe, the peaks are found to be situated in-between that of LFCO and LCCO. This is expected due to the lower Fe content and the smaller ionic radius of Cr³⁺ in comparison. Safakas et al. showed a similar trend when the relative amount of Fe³⁺ in LaFe_{1-x}Co_xO_{3-δ} was decreased and a contraction effect on the unit cell was present due to the lower Fe³⁺:Co³⁺ ratio [42]. These corresponding shifts reinforce the successful substitution of dopants into the B-site. Furthermore, the decrease in crystalline sizes on substitution can be related to the decrease in the unit cell volume and micro-strain [67].

Rietveld refinement of the representative LaCr_{0.25}Fe_{0.25}Co_{0.5}O_{3-δ} composition was carried out by GSAS and EXPGUI [71,72]. The refined XRD pattern is shown in Fig. S1 with the lattice parameters are listed in Table 2. It has been confirmed that LFCO exhibit a hexagonal structure with space group R-3c (167); $a = 5.4786(1)$ Å, $c = 13.2100(2)$ Å and $V = 343.378(6)$ Å³. It should be noted that all lattice parameters are within a similar range to the parent structure and as expected, the unit

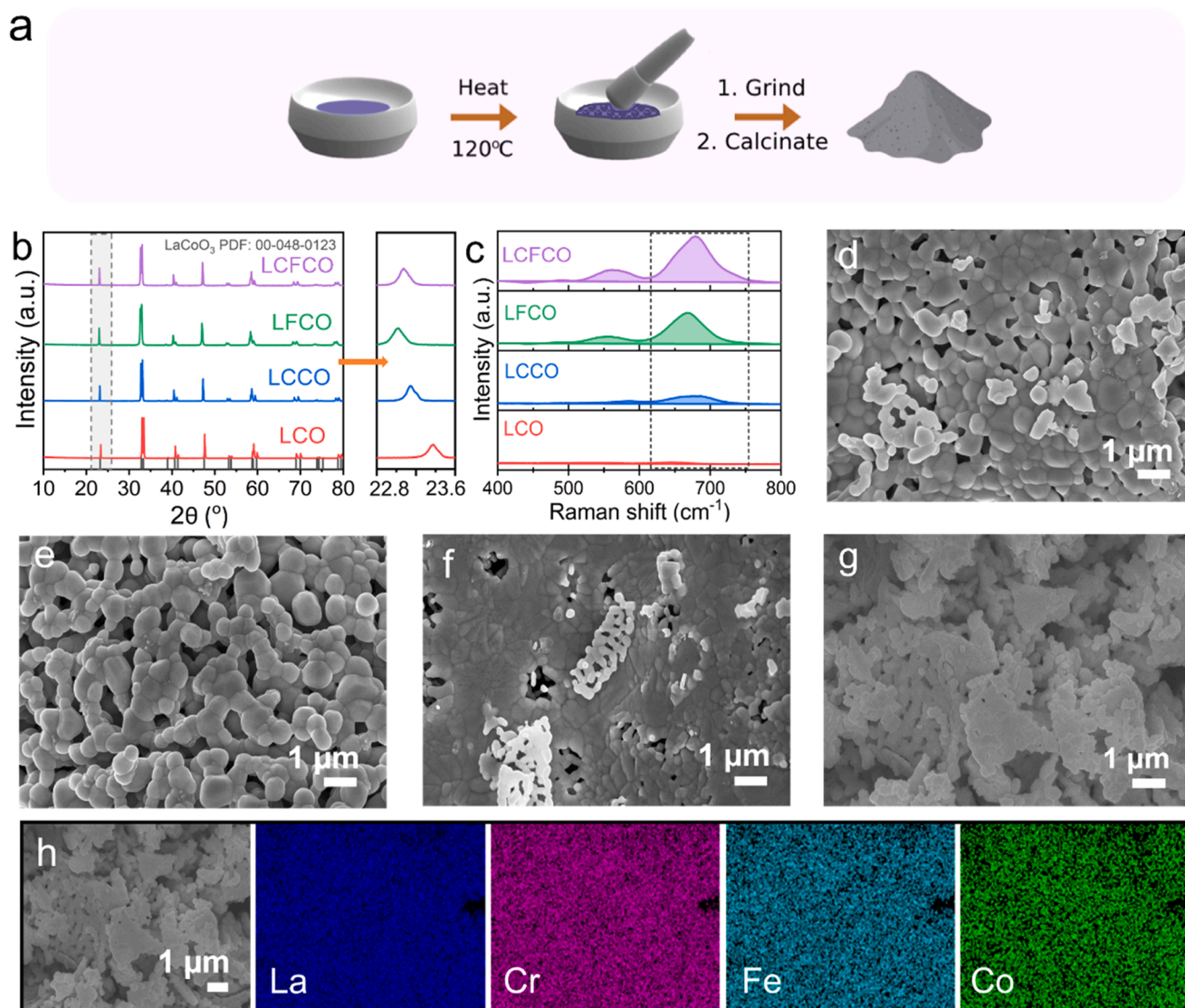


Fig. 1. (a) Schematic illustration of the preparation process of LCO-based perovskite powders by combustion method. (b) X-ray powder diffraction (XRD) patterns of the prepared LCO, LCCO, LFCO and LCFCO perovskite powders; XRD patterns in the 2θ range 22.8 – 23.6° (right). (c) Raman spectra of LCO, LCCO, LFCO and LCFCO. SEM images of (d) LCO (e) LCCO (f) LFCO and (g) LCFCO at mag $\times 10K$. (h) SEM and corresponding EDS elemental mappings of La, Cr, Fe and Co in LCFCO at mag $\times 10K$.

Table 1

Structural features of synthesised perovskite oxides.

Perovskite	Crystal system	a (Å)	c (Å)	Unit cell volume (Å ³)	Crystallite size (nm) ^a	Crystallite size (nm) ^b
LaCoO _{3-δ}	Rhombohedral	5.4364(4)	13.0822(3)	334.83	44.5	74.5
LaCr _{0.5} Co _{0.5} O _{3-δ}	Rhombohedral	5.4717(5)	13.1696(9)	341.47	41.6	63.9
LaFe _{0.5} Co _{0.5} O _{3-δ}	Rhombohedral	5.4825(9)	13.2286(8)	344.35	29.2	59.9
LaCr _{0.25} Fe _{0.25} Co _{0.5} O _{3-δ}	Rhombohedral	5.4786(1) ^c	13.2100(2) ^c	343.38(6) ^c	36.4	62.7

^a crystal size was calculated by Scherrer equation.

^b crystal size was calculated by the Williamson-Hall plot method.

^c lattice parameter and unit cell volume calculated from Rietveld refinement method.

cell volume of LCFCO (343.38 Å^3) is between that of LFCO (344.35 Å^3) and LCCO (341.47 Å^3). The refined parameters therefore support the above analysis indicating successful substitution into the B-site.

Raman spectroscopy was used to gain greater insight into the M-O bond strength for the perovskite powders. The four distinguishable bands present for LaCoO₃ in Fig. 1c coincide with those stated in literature [66,73,74]. The band that appears at the lowest Raman shift value is associated with the E_g La stretching vibration [74]. There is minimal

shift in this band on substitution at the B-site which indicates that the introduction of Cr and Fe dopants do not interact with the A-site but instead engage at the B-site. The second and third bands are due to the E_g bending and E_g quadrupole vibrations respectively. The highest energy band is attributed to the A_{2g} breathing mode of the oxygen ion cage with respect to the CoO₆ octahedron [74]. These latter bands associated with CoO₆ vibrations are shown to be more sensitive to B-site substitution as expected. The A_{2g} band in LCO has the lowest Raman energy (642 cm^{-1}).

Table 2

Structure and lattice parameters of $\text{LaCr}_{0.25}\text{Fe}_{0.25}\text{Co}_{0.5}\text{O}_{3-\delta}$ determined by Reitveld refinement.

Atom	Site	Occupancy	x	y	z	$U_{\text{iso}}(\text{\AA}^2)$
La	6a	1	0	0	1/4	0.0154(3)
Cr	6b	0.25	0	0	0	0.0132(5)
Fe	6b	0.25	0	0	0	0.0132(5)
Co	6b	0.5	0	0	0	0.0132(5)
O	18e	0.984(6)	0.4465(4)	0	0	0.0186(14)

Space group $R\bar{3}c$ (167); $a = 5.4786(1) \text{\AA}$, $c = 13.2100(2) \text{\AA}$, $V = 343.378(6) \text{\AA}^3$, $Z=6$, $R_{\text{wp}} = 9.84\%$, $R_p = 7.84\%$, $\chi^2 = 2.495$.

In the presence of B-site substitution, the A_2g band shifts to higher Raman energies for LCCO and LFCO (681 cm^{-1} and 667 cm^{-1} respectively). The A_2g band in LCFCO is found in-between that of the above-mentioned, with a Raman energy of 678 cm^{-1} , revealing that the Co B-site interacts with both Cr and Fe. The absence of additional bands and the respective shifting of the A_2g band indicates that the dopants are successfully introduced into the BO_6 octahedron, in agreement with XRD.

The morphologies of the prepared perovskite powders were characterised by SEM. The images in Fig. 1d-g reveal globular grains are formed for all compositions which are relatively uniform in size. It should also be noted that an obvious reduction in grain size is observable as Fe is introduced into the sample. This has been reported in literature where the presence of Fe reduces the extent of particle agglomeration [70]. EDS was used to explore the different elemental compositions and a detailed analysis is reported in Table S1. Elemental mapping of the LCFCO perovskite is also provided to demonstrate visual distribution of the elements against the scale bar given in Fig. 1h. The elements of La, Fe, Cr and Co are homogeneously dispersed with no apparent areas of agglomeration, this is in agreement with the formation of a single-phase perovskite with no bulk impurities.

The nature and surface composition of the samples were studied by XPS. The spectrum of LCFCO (Fig. 2a-d), LCO, LCCO and LFCO (Fig. S2,

S3 and S4 respectively) are provided. Since the data can be fitted well to the La_2O_3 spectra, the La species present at the A-sites are reasonably assumed to be in the +3 oxidation state as expected, satisfying the ABO_3 composition. The deconvoluted spectra can be fitted to peaks arising from La $4d_{5/2}$ and La $4d_{3/2}$ [75]. The Co $2p_{3/2}$ peaks of all samples can be fitted well to the Co_3O_4 spectra [76]. It is stated in literature that for Co_3O_4 , where Co(II/III) exists in the +2 and +3 oxidation states, the Co $2p_{3/2}$ peak corresponding to binding energies (BE) around 780 eV can be assigned to octahedral Co^{3+} , whereas the Co $2p_{3/2}$ signal at higher BE, at around 781 eV, together with the shake-up satellite signals are indicative of surface Co^{2+} [77–79]. The results therefore suggest the presence of Co in both the +2 and +3 oxidation states in all samples. Furthermore, the Co $2p_{3/2}$ peak observed at higher BE may be closely related to the CoO species where Co is in the +2 oxidation state [76]. The peak with lowest BE in all spectra can therefore be associated with Co in the +3 oxidation state whilst the latter two peaks at higher BE may be assigned to the +2 oxidation state. The deconvoluted Cr $2p_{3/2}$ spectra in LCCO and LCFCO are characteristic of Cr^{6+} and Cr^{3+} species [77]. The fractional percentage of Cr in the +3 oxidation state is calculated to be around 56.9% in LCFCO, which is similar to that of LCCO (61.9%) (Table S2). This demonstrates that the fraction of Cr^{3+} species within the sample remains relatively unchanged in the presence of additional dopants. Furthermore, the Fe $2p_{3/2}$ and $2p_{1/2}$ spectra can be fitted to peaks corresponding to Fe_2O_3 where Fe is in the +3 oxidation state. On introduction of Cr into LCO, there is a clear shift of the Co $2p_{3/2}$ peak position towards higher binding energies from 779.7 eV to 780.4 eV, as well as an obvious increase in satellite signal intensity, both of which are indications of strong interactions between Cr and Co [77]. There is also an increase in binding energy of the Co $2p_{3/2}$ profile when Fe is introduced into LCO to form LFCO (779.9 eV), however, this is not as pronounced, indicating Cr may interact more strongly with the Co centre. When both Fe and Cr are introduced, LCFCO also demonstrates a shift in Co $2p_{3/2}$ peak position towards a binding energy of 780.0 eV. These results demonstrate that in the presence of both dopants, the surface species do not change and there are no further variations in oxidation states. Through slight changes in binding energy however, it can be

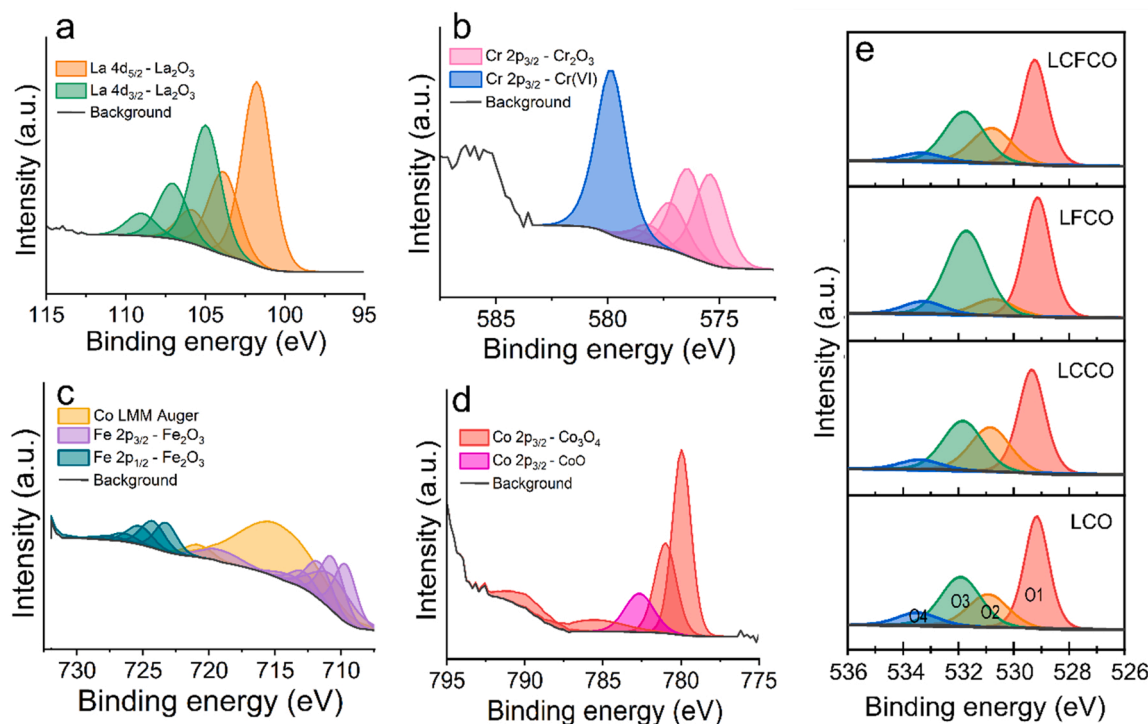


Fig. 2. XPS analysis of LCFCO demonstrating (a) La (b) Cr (c) Fe and (d) Co spectra. (e) Deconvoluted O 1s spectra for the LCO, LCCO, LFCO and LCFCO perovskite powders.

deduced that these ions interact at the B-site which may lead to synergistic effects.

The surface oxygen species at the surface of the perovskite powders were also investigated by XPS (Fig. 2e). The spectra can be fitted into four subpeaks that can be assigned to the lattice oxygen species (O^{2-}), highly oxidative oxygen species (O_2^2/O^-), surface-adsorbed oxygen species or hydroxyl groups (OH^-) and surface adsorbed water (H_2O) labelled as O1, O2, O3 and O4 respectively [48,80]. The relative concentration of each oxygen-containing species is listed in Table S3. According to literature, the highly oxidative oxygen species (O_2^2/O^-) is closely related to surface oxygen vacancies and defects [48,80–82]. Compared to LCO, incorporation of Cr in LCCO results in an increase in the O2 peak, indicating an enhancement in surface oxygen vacancies. When Fe is introduced however, this is much less pronounced. LCFCO also shows a relative increase in surface oxygen vacancy ratio.

Since LCFCO is a new perovskite, its synthesis methods have not been widely explored. The synthesis method of LCFCO was therefore studied to assess the limits and properties of the perovskite at varying calcinating temperatures. LCFCO was prepared at different temperatures of 600, 700, 800 and 900 °C labelled as LCFCO-600, LCFCO-700, LCFCO-800 and LCFCO-900 respectively. The corresponding XRD analysis for these powders is shown in Fig. 3. For comparison, the parent LCFCO (LCFCO prepared at 1000 °C) perovskite sample is also displayed.

The major differences found by XRD analysis between the samples are: (i) LCFCO-700 has broader peaks compared to its counterparts indicating smaller particle size and (ii) sample LCFCO-600 contains a secondary phase which is reflected by an additional reflection at a 2θ value of 28.4° belonging to the (040) plane of La_2CoO_4 (PDF 04–008–9324) whereas samples LCFCO-700, LCFCO-800 and LCFCO-900 are single phase. Nevertheless, the results imply that the perovskite only becomes single phase at temperatures above 700 °C. For this reason, only LCFCO-700, LCFCO-800 and LCFCO-900 are considered as potential ORR catalysts.

To get a better idea of size-activity relationship, it is important to

explore crystal sizes of the LCFCO based samples. Table 3 shows the crystallite domains for the LCFCO-700, LCFCO-800, LCFCO-900 and parent LCFCO perovskite samples calculated from both the Scherrer equation and Williamson-Hall relationship. The data reveals that there is an obvious reduction in crystalline size as calcinating temperature is reduced. These results are consistent with literature [29].

The methods above give an average value of crystalline domain size of the grains; however, real samples tend to have grains with different domains. To assess the distribution of different grain sizes and explore the morphologies of the prepared perovskite powders, SEM characterisation was used. The images in Fig. 3b–d reveal an obvious reduction in grain size as calcinating temperature is reduced, with LCFCO-700 showing a distinctively small grain size. This coincides with the analysis obtained from XRD.

The measured specific surface areas (SSA) of the synthesised perovskite powders ranged from 1.0 to $5.2\text{ m}^2\text{g}^{-1}$ as shown in Table 3. Such SSA values are typical for perovskites due to the relatively high temperature treatment required to form single phase perovskite oxides

Table 3

Particle sizes and specific surface area (SSA) of the synthesised perovskite oxides.

Perovskite	Crystal system	Crystallite size (nm) ^a	Crystallite size (nm) ^b	SSA (m^2g^{-1})
$LaCr_{0.25}Fe_{0.25}Co_{0.5}O_{3-\delta}$ -700	Rhombohedral	24.6	57.1	5.2
$LaCr_{0.25}Fe_{0.25}Co_{0.5}O_{3-\delta}$ -800	Rhombohedral	29.49	49.2	2.1
$LaCr_{0.25}Fe_{0.25}Co_{0.5}O_{3-\delta}$ -900	Rhombohedral	34.2	61.2	1.2
$LaCr_{0.25}Fe_{0.25}Co_{0.5}O_{3-\delta}$	Rhombohedral	36.4	62.7	1.0

^a crystal size was calculated by Scherrer equation.

^b crystal size was calculated by the Williamson-Hall plot method.

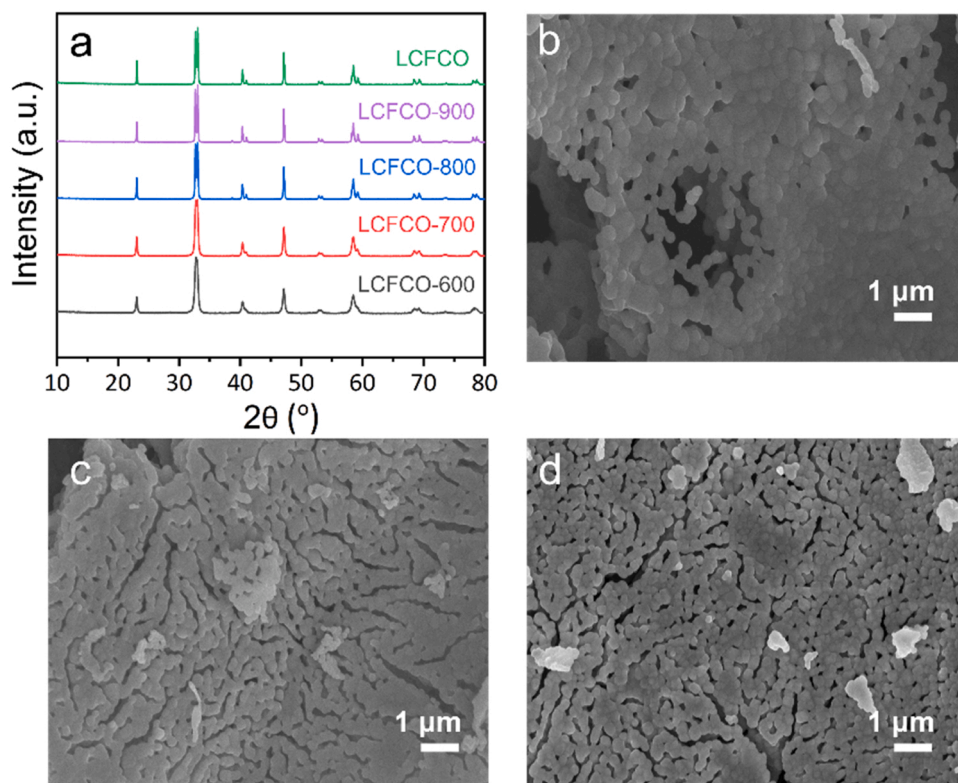


Fig. 3. (a) X-ray powder diffraction (XRD) patterns of the prepared LCFCO-600, LCFCO-700, LCFCO-800, LCFCO-900 and LCFCO perovskite powders. SEM images of (b) LCFCO-900 (c) LCFCO-800 and (d) LCFCO-700 at mag x10K.

[29,42].

There is a clear increase in SSA as calcining temperature is reduced, which is in accordance to literature [29]. The results can be rationalised due to higher calcining temperatures resulting in the agglomeration of particles and consequently smaller exposed surface areas. The development of synthesis methods leading to reduced particle sizes, and therefore an increased SSA, could allow for the same ORR performance to be obtained at a lower cathode loading. This indicates that a smaller cathode layer thickness can be utilised and for reduced voltage losses due to mass transport resistances [42,83].

3.2. Evaluation of oxygen reduction reaction

The electrocatalytic performance of the LCO, LFCO, LCCO and LCFCO perovskite samples towards ORR were evaluated in O₂-saturated 0.1 M KOH solution between -0.6 and 0.1 V vs. Ag/AgCl (0.36–1.06 V vs. RHE) at a scan rate of 10 mVs⁻¹. The potential range was chosen to avoid possible irreversible reduction of the perovskite catalysts by avoiding more cathodic potentials being applied. For comparison, the polarisation curve for the Pt/C electrocatalyst was also collected under similar conditions.

Fig. 4a illustrates the comparative current density (normalised to the geometric surface area of the electrode disk) vs. potential for the electrocatalysts with a rotation rate of the RDE equal to 1600 rpm. Furthermore, polarisation curves for the electrocatalysts over rotation rates of 100, 400, 900 and 1600 rpm are shown in Fig. 4b and Figs. S5a–c. Over the entire potential range, the current density at the same potential increases upon doping at the B-site, indicating an increase in ORR activity. Though, it is difficult to draw definite conclusions without further analysis since the reduction reaction depends on several factors.

An overview of the intrinsic ORR activity for electrocatalysts can be inferred from their onset potentials [20,42]. The onset potentials E_{onset} of the perovskites were determined by intersection of the current baseline and a tangent line drawn from the polarisation curve at the end of the kinetic control region (Fig. S6a) [42]. On this basis, the onset potentials of the electrocatalysts follows the descending order LCFCO > LFCO > LCCO > LCO with E_{onset} values of 0.97 > 0.95 > 0.83 > 0.80 V vs. RHE respectively. The onset potential of LCFCO shows similar performance to the Pt/C electrocatalyst (0.96 V vs. RHE) (Fig. 4d). This value is similar to that of PGM-based electrocatalysts reported in literature, whereby ORR onset potentials more positive than 0.93 V vs. RHE have been recorded for both Pt/C (20 wt%) and Pd/C (20 wt%) in alkaline medium [20,84,85]. Notably, the onset potential of the LCFCO electrocatalyst can be deduced as being heavily influenced by the presence of Fe, since LFCO shows a similar positive shift in onset potential compared to undoped LCO. Introduction of Cr in LCCO shows a much less pronounced shift. A similar positive shift in ORR onset potential when Fe is introduced into electrocatalysts has been reported in literature [84,85].

One of the most common methods for evaluating catalyst performance is to compare half-wave potentials $E_{1/2}$. This is particularly useful as it allows for PGM-free electrocatalysts to be compared with Pt catalysts in terms of their half-wave potential [86]. The $E_{1/2}$ values of the perovskites were determined by the potential recorded at the midpoint of the polarisation curves; the point at which the reduction current begins rapidly increasing and saturation in the limiting region (Fig. S6b). On this basis, the half-wave potential of the electrocatalysts follows the descending order LFCO > LCFCO > LCCO > LCO with $E_{1/2}$ values of 0.87 > 0.86 > 0.71 > 0.68 V vs. RHE. Despite the $E_{1/2}$ value for LFCO being slightly greater than that of LCFCO, the change is minimal, and

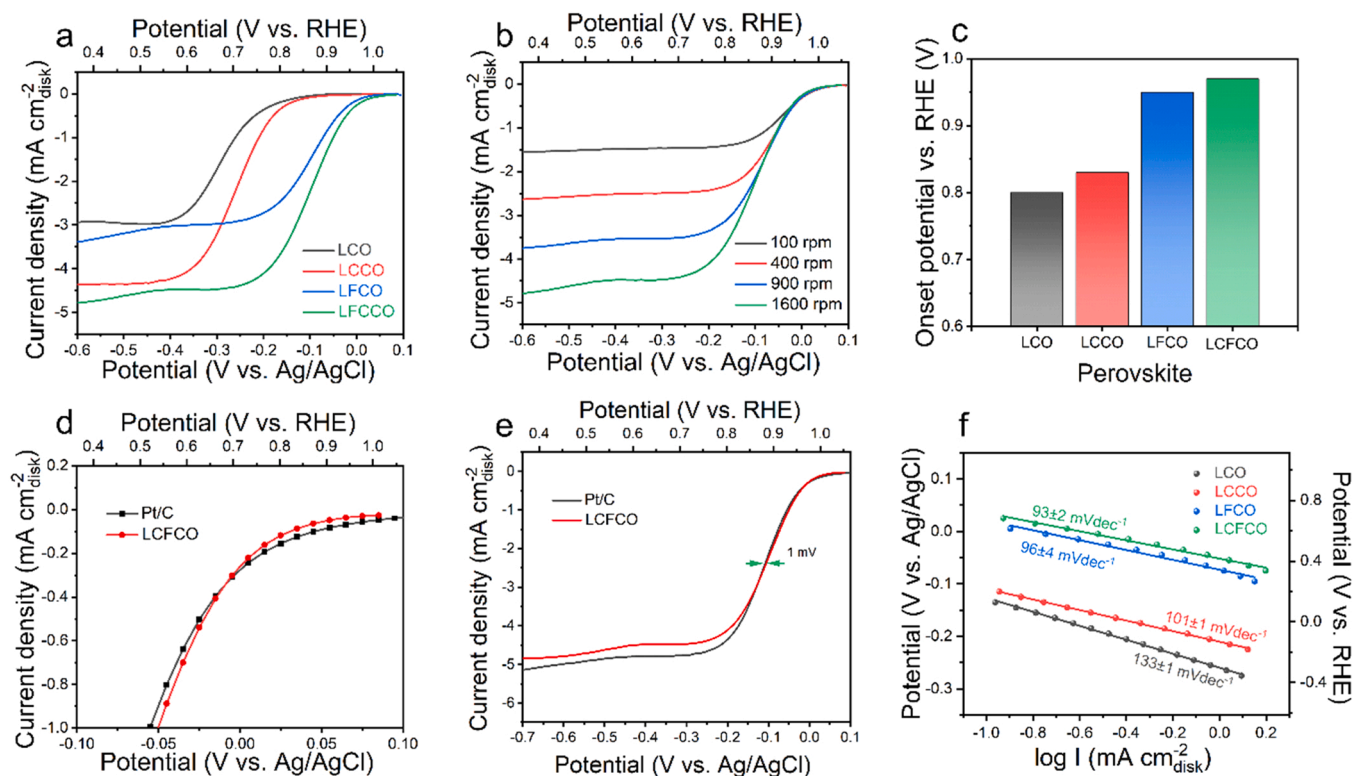


Fig. 4. (a) Polarisation curves obtained for the LCO, LCCO, LFCO and LCFCO perovskites in O₂-saturated 0.1 M KOH solution; RDE rotation rate of 1600 rpm. (b) Polarisation curves of the LCFCO perovskite in O₂-saturated 0.1 M KOH solution; RDE rotation rates of 100, 400, 900 and 1600 rpm. (c) Onset potential values for the tested electrocatalysts in O₂-saturated 0.1 M KOH solution and room temperature; RDE rotation rate of 1600 rpm. (d) Comparison of the onset potential E_{onset} between the Pt/C and LCFCO in O₂-saturated 0.1 M KOH solution. (e) Zoomed comparison of the onset potential E_{onset} between the Pt/C and LCFCO electrocatalysts with half-wave potential $E_{1/2}$ difference noted in O₂-saturated 0.1 M KOH solution; RDE rotation rate of 1600 rpm. (f) Corresponding Tafel plots for ORR on the LCO, LCCO, LFCO and LCFCO perovskites in O₂-saturated 0.1 M KOH solution.

both show a substantial difference compared to the undoped LCO. The half-wave potential value of LCFCO is comparative to Pt/C and other PGM-free electrocatalysts reported in literature, which fall in the range between 0.53 and 0.87 V vs. RHE [84,86–91]. Furthermore, Pt/C in this study showed a slightly lower half-wave potential of 0.85 V vs. RHE (Fig. 4e). Tran et al. recorded a similar $E_{1/2}$ of 0.84 V vs. RHE for Pt/C in O_2 -saturated 0.1 M KOH solution with a RDE rotation rate of 1600 rpm [84]. This illustrates the great potential of LCFCO as a PGM-free electrocatalyst for ORR.

To gain further insight into the ORR kinetics, Tafel plots were constructed and fitted for the perovskite electrocatalysts (Fig. 4f). The Tafel slope for LCFCO (93 mVdec^{-1}) is smaller than LFCO, LCCO and LCO (99, 101 and 133 mVdec^{-1} respectively), indicating that the incorporation of the Cr and Fe dopants into LCO induces faster electrokinetics.

As well as improved onset potential and half-wave potential, the LCFCO electrocatalyst also shows an enhanced current density at the same potential over the same range compared to the undoped and singly doped counterparts (Fig. 5a). The enhanced ORR activity cannot therefore be merely described by differences in E_{onset} and $E_{1/2}$. Fig. 5b shows Koutecky-Levich (K-L) plots for the electrocatalysts at an applied potential of $-0.55 \text{ V vs. Ag/AgCl}$ (0.41 V vs. RHE) using polarisation data obtained in Fig. 4b and Figs. S5a–c. The data corresponding to each electrocatalyst falls on a straight line thus indicating that Eq. (3) is satisfied. From the slope of the line and application of Eq. (4), the number of transferred electrons n per reduced oxygen molecule can be calculated. The results of this calculation are visually presented in Fig. 5c. The number of electrons involved in the ORR mechanism changes on introduction of dopants indicating a corresponding change in the ORR pathway for the different electrocatalysts. The calculated average number of transferred electrons n follows the ascending order of $3.2 < 3.4 < 3.8 < 4.0$ for $\text{LCO} < \text{LFCO} < \text{LCCO} < \text{LCFCO}$. It is evident

that the presence of Cr plays a key role in increasing the number of electrons involved in the ORR mechanism and therefore play a key role in the improved current density of LCFCO compared to undoped LCO. This may be partly attributed to the oxygen species present on the surface of the perovskite [85]. Oxygen vacancy formation at the perovskite surface has been reported to promote oxygen adsorption and charge transfer [21,42,82]. Several studies have reported the beneficial effects of surface oxygen vacancies on the ORR activity of perovskites as well as selectivity to the $4e^-$ reduction pathway [21,42,82,92–95]. XPS analysis in Fig. 2e reveals that the mass percent of O_2^{2-}/O^- (O_2) is higher in both LCCO and LCFCO than in LCO. As mentioned above, literature shows that this highly oxidative oxygen species (O_2^{2-}/O^-) is closely related to surface oxygen vacancies and defects [48,80–82]. This can therefore be used as an indication of oxygen vacancy content present within the samples studied. The respective ratio of $O_2/(O_1 + O_3 + O_4)$ was subsequently calculated to give an estimated oxygen vacancy ratio and is visually displayed in Fig. 5d [48,80,81]. On introduction of Fe, LFCO displays a lower area ratio (9%), which is indicative of a lower oxygen vacancy ratio, and minimal change in current density at the same potential over the same potential range compared to LCO. Similar trends in oxygen vacancy formation have been observed in literature [21,42,96]. Garcia-Lopez et al. for example, found a decrease in oxygen vacancy ratio with increasing substitution of Co by Fe in $\text{La}_{0.6}\text{Sr}_{0.4}\text{Fe}_{1-x}\text{Co}_x\text{O}_{3-\delta}$ [96]. Moreover, on introduction of Cr, LCCO shows a much greater increase in oxygen vacancy ratio (34%) and current density at the same potential over the same potential range compared to LCO (24%). The results imply that oxygen vacancy formation at the LCFCO surface (27%) is heavily influenced by the presence of Cr. Gao similarly reported that when introducing Cr doping, the $\text{LaCr}_{0.25}\text{Fe}_{0.25}\text{O}_3$ perovskite possessed a higher ratio of oxygen defects, O_2 (48.4%), than other samples studied [81]. It is therefore deduced that the presence of the Cr introduced more

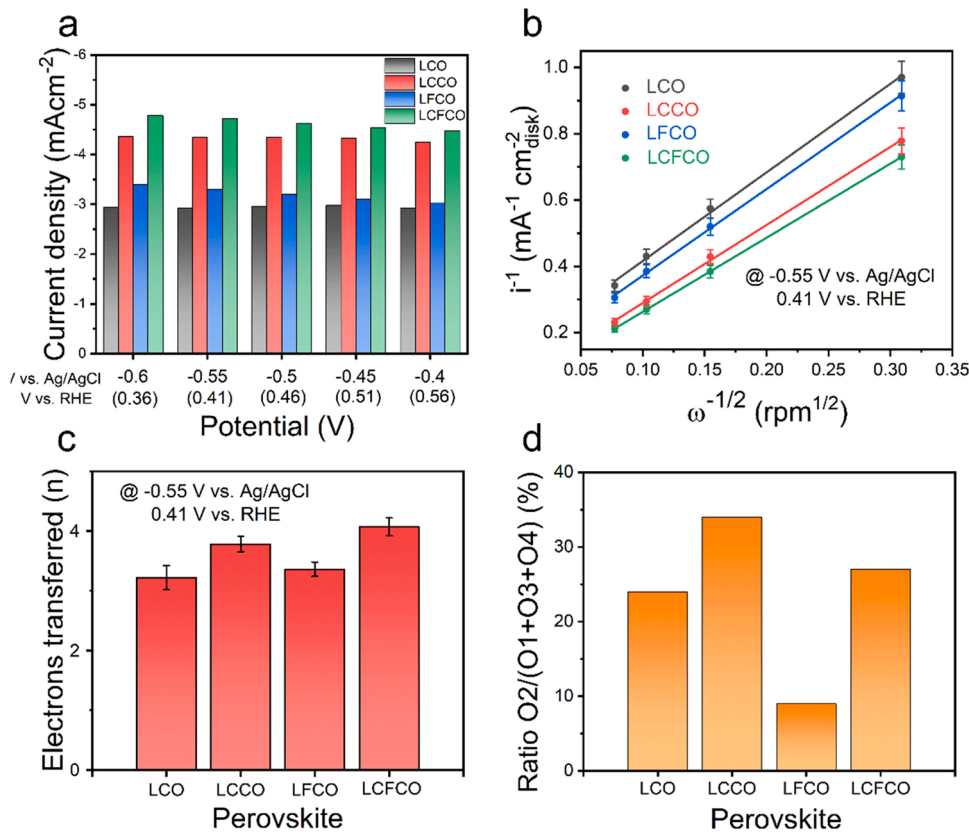


Fig. 5. (a) Bar graphs showing the tested LCO, LCCO, LFCO and LCFCO electrocatalyst current density responses at selected potentials. (b) Koutecky-Levich (K-L) plots for the LCO, LCCO, LFCO and LCFCO perovskites at a potential of $-0.55 \text{ V vs. Ag/AgCl}$ (0.41 V vs. RHE). (c) Calculated electron transfer number n for ORR using K-L slopes. (d) Area ratio $O_2/(O_1 + O_3 + O_4)$ in the tested electrocatalysts as deduced from XPS analysis.

oxygen defects, in turn enhancing OER activity and the interaction of adsorbed oxygen-containing species. It can subsequently be assumed that the presence of Cr doping can lead to oxygen vacancies which increase ORR activity and selectively favour the $4e^-$ reduction pathway.

Apart from electrocatalytic activity, stability is another important factor for advanced electrocatalysts. The long-term stability of the LCFCO was confirmed by chronopotentiometry tests in O_2 -saturated 0.1 M KOH solution at a fixed potential of -0.4 V vs. Ag/AgCl with a RDE rotation rate of 1600 rpm. As shown in Fig. 6a, LCO shows a decrease in stability over the testing duration. However, with the doped perovskites and particularly the LCFCO electrocatalyst, there is an initial slight decrease during testing which then stabilises over the duration. The relative current density of LCFCO reaches around 94.5% throughout the testing period, indicating that the electrocatalyst remains stable over an extended period. Notably, the stability of LCFCO is slightly higher than that of Pt/C over the same testing duration and conditions (Fig. 6b). Similar stability of Pt/C (20 wt%) electrocatalysts has been observed in literature, where a retention of 93.5% was observed after 10000 s in O_2 -saturated 0.1 M KOH solution with a RDE rotation rate of 1600 rpm [85]. The results indicate that LCFCO is a highly active and stable electrocatalyst towards ORR.

As mentioned in previous studies, ORR on perovskite oxides in alkaline media is complicated and the reaction depends on several factors such as intrinsic activity, conductivity and surface adsorption properties, all of which should not be considered independently [20,42]. Changes in electronic structure can affect the rate determining steps and the overall ORR activity. Suntivich et al. recently proposed that the electronic configuration and e_g orbital filling at the B-site of the perovskite can effectively be used as an activity descriptor for ORR [23, 57]. It was determined that a maximum ORR activity was observed when the e_g -filling was close to 1. This concept has been applied to pioneer successful perovskites electrocatalysts towards ORR activity such as $LaMn_{0.3}Co_{0.7}O_3$, $LaCo_{1-x}Ni_xO_{3-\delta}$, $La_{0.8}Sr_{0.2}Mn_{1-x}Ni_xO_3$, $LaNi_{1-x}Mg_xO_3$ and $LaNi_{1-x}Fe_xO_3$ [48,49,97–99].

Since the exact spin states of the transition metals in $LaCr_{0.25}Fe_{0.25}Co_{0.5}O_{3-\delta}$ have not been determined prior to this study, an approximation of the e_g filling based on literature and XPS data provided in Table S2 has been made. Given that the B-site metal exhibits different valence states, the electronic filling of the e_g orbital becomes complex. It is often widely accepted that Co^{2+} (d^7) ions exist in high spin states ($e_g = 2$), whereas the spin state of Co^{3+} in $LaCoO_3$ has proven to be more difficult to determine. It is often accepted that Co^{3+} exists in an intermediate-spin (IS) state at temperatures above 70–90 K, rather than the Hund's predicted high-spin (HS) state ($t_{2g}^4e_g^2$) [66,100,101]. It is due to this phenomenon that Co^{3+} in $LaCoO_3$ is assumed to have unique

electronic properties where the e_g occupancy is ~ 1 . Although there is still extensive debate over Co spin state, Co^{3+} is assumed to exist in an intermediate spin state ($e_g \sim 1$) for the simplicity of the calculations in this study [100–104]. Based on literature, Fe^{3+} tends to favour high spin configuration ($t_{2g}^3e_g^2$), leading to an e_g filling of 2. Furthermore, XPS data also reveals that Cr in LCCO and LCFCO exists in the $+6$ and $+3$ oxidation state, with the latter being dominant. For e_g calculations, the effect of Cr^{6+} are neglected since there are no d electron orbitals and only Cr^{3+} ($t_{2g}^3e_g^0$) is considered, leading to an e_g filling of 0. The average filling of electrons in the e_g orbital (n) can be calculated based on Eq. (S4) [48]. From the calculations, it can be seen that the e_g filling of LCO was around $e_g = 1.5$ and approaches closer to 1 when doped by both Cr and Fe in LCFCO where $e_g = 1.16$. The near unity e_g -filling found in LCFCO may also partially explain the enhanced ORR activity compared to its undoped and singly doped counterparts.

Furthermore, the electrocatalytic performance of the LCFCO-700, LCFCO-800 and LCFCO-900 perovskite samples towards ORR were evaluated in O_2 -saturated 0.1 M KOH solution between -0.6 and 0.1 V vs. Ag/AgCl (0.36 – 1.06 V vs. RHE) at a scan rate of 10 mVs $^{-1}$ (Fig. 7a and Figs. S7a–b). The potential range was chosen to avoid possible irreversible reduction of the perovskite catalysts by avoiding more cathodic potentials being applied. For comparison, the polarisation curves for the parent LCFCO perovskite sample and Pt/C electrocatalyst are also displayed in Fig. 7b and c respectively.

Fig. 7b illustrates the comparative current density (normalised to the geometric surface area of the electrode disk) vs. potential for the LCFCO-700 and LCFCO electrocatalysts with a rotation rate of the RDE equal to 1600 rpm. The key differences between the samples are: (i) LCFCO-700 shows a more positive E_{onset} potential compared to LCFCO, (ii) LCFCO shows a more positive $E_{1/2}$ potential (0.88 V vs. RHE) compared to LCFCO (0.86 V vs. RHE) and (iii) LCFCO-700 shows a slight increase in current density (-4.85 mAcm $^{-2}_{disk}$) compared to LCFCO (-4.77 mAcm $^{-2}_{disk}$) at a reducing potential of -0.6 V vs. Ag/AgCl (0.36 V vs. RHE). These improvements in performance may be attributed to the enhancement in the number of exposed active sites due to a higher SSA. Similar trends have been seen by Retuerto et al. who found that perovskite catalysts 700-LaNiO $_3$ and 800-LaNiO $_3$, which were calcinated at 700 and 800 °C respectively, showed more positive E_{onset} potentials than 900-LaNiO $_3$ and 1000-LaNiO $_3$, which were calcinated at 900 and 1000 °C respectively [29]. Moreover, Fig. 7c shows that LCFCO-700 has similar enhancement in E_{onset} and $E_{1/2}$ potentials compared to commercial Pt/C. Furthermore, the current density value is remarkably similar to the commercial Pt/C electrocatalyst, illustrating that LCFCO-700 is a promising candidate for ORR.

Amongst AEMFCs, direct ammonia fuel cells (DAFCs) have becoming

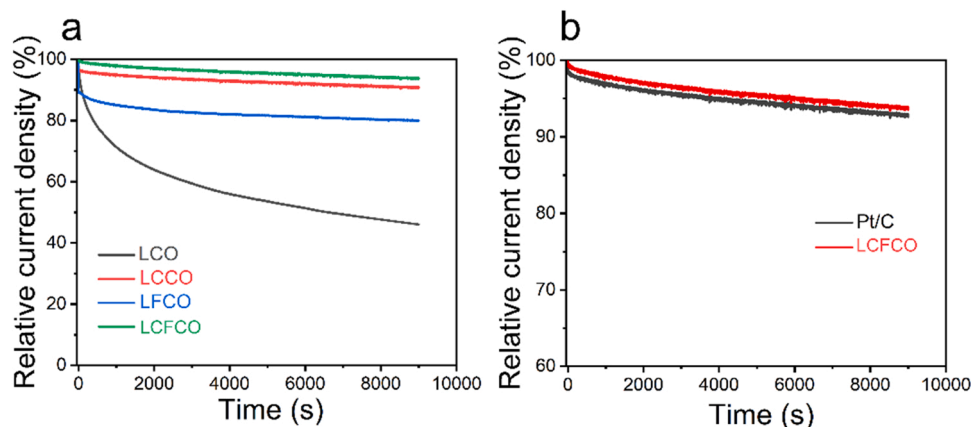


Fig. 6. (a) Chronopotentiometry analysis of the LCO, LCCO, LFCO and LCFCO perovskites held at a fixed potential of -0.4 V vs. Ag/AgCl in O_2 -saturated 0.1 M KOH solution; RDE rotation rate of 1600 rpm. (b) Chronopotentiometry analysis of the Pt/C and LCFCO electrocatalysts held at a fixed potential of -0.4 V vs. Ag/AgCl in O_2 -saturated 0.1 M KOH solution.

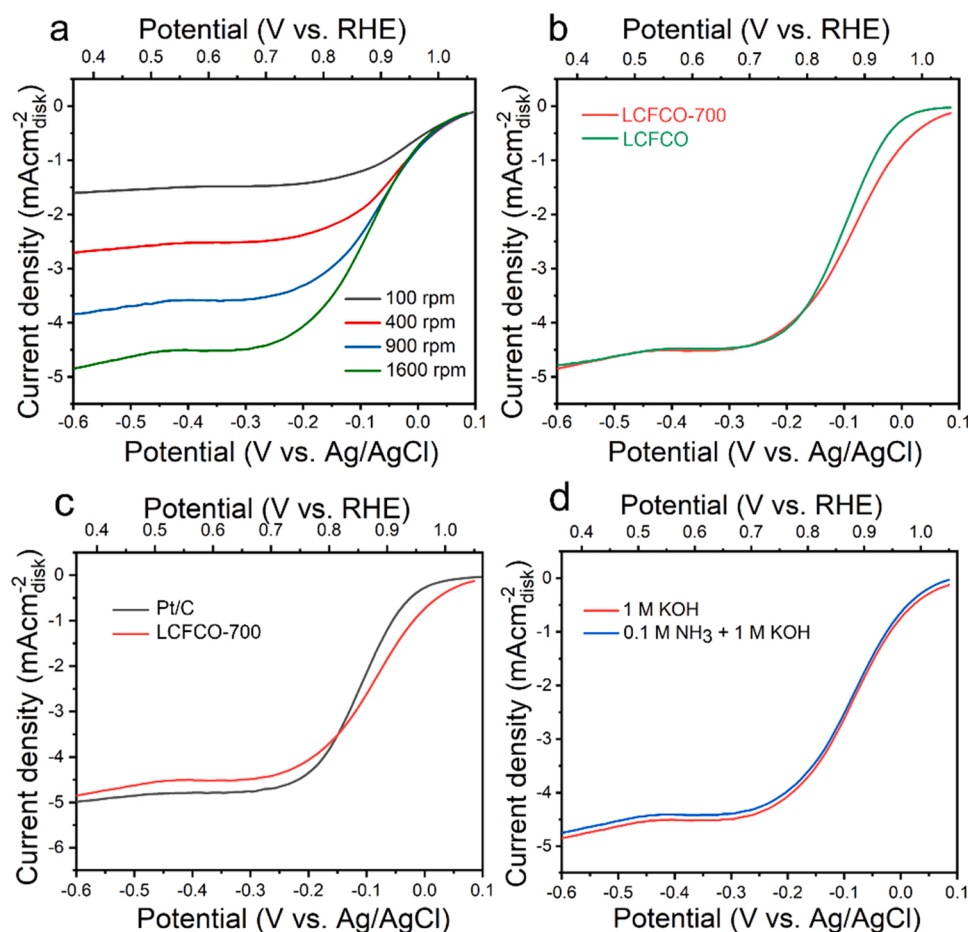


Fig. 7. (a) Polarisation curves of the LCFCO-700 perovskite in O_2 -saturated 0.1 M KOH solution; RDE rotation rates of 100, 400, 900 and 1600 rpm. (b) Polarisation curves obtained for the LCFCO-700 and LCFCO perovskites in O_2 -saturated 0.1 M KOH solution; RDE rotation rate of 1600 rpm. (c) Polarisation curves of Pt/C and LCFCO-700 electrocatalysts in O_2 -saturated 0.1 M KOH solution; RDE rotation rate of 1600 rpm. (d) Polarisation curves obtained for the LCFCO-700 in O_2 -saturated 0.1 M KOH solution with and without 0.1 M NH_3 ; RDE rotation rate of 1600 rpm.

increasingly popular due to the fuel's high energy density, large-scale global production, extensive existing infrastructure, and low cost per unit energy [1,31–36,38]. These systems employ electrocatalysts at the anodic and cathodic site that can assist the ammonia oxidation reaction (AOR) and oxygen reduction reaction (ORR) respectively. The choice of a cathode catalyst for DAFCs has been directed by: (i) the desire to reduce use of PGMs and (ii) a minimal impact on ORR activity in the presence of ammonia [105]. The latter stems from the acknowledgement that ammonia crossover to the cathode is common in existing in DAFCs based on polymeric membrane electrolytes [1, 105]. This study has shown how the first directive is satisfied; avoiding reliance on PGMs and making use of a cheaper, more readily available LCFCO-700 perovskite oxide that shows comparable ORR activity to commercial Pt/C. To satisfy the second requirement, that being a minimal impact on ORR activity in the presence of ammonia, the LCFCO-700 perovskite oxide was tested in O_2 -saturated 0.1 M KOH solution with and without the presence of 0.1 M NH_3 to mimic the effects of ammonia fuel cross over in a fuel cell. Fig. 7d shows that on introduction of 0.1 M NH_3 , there is negligible change in ORR activity for the LCFCO-700 perovskite oxide, indicating that the ORR activity is not affected by the presence of a small amount of ammonia. It can therefore be reasonably assumed that there will be minimal negative effect of ammonia cross-over if LFCCO-700 were to be employed as a cathode in a DAFC, making it a suitable and promising non-noble cathode candidate.

4. Performance of direct ammonia fuel cells

Due to its promising activity towards ORR and minimal change in the presence of ammonia, LCFCO-700 was considered as a suitable cathode in a DAFC. To assess the performance of the perovskite oxide, a catalyst

ink was prepared and brushed onto carbon cloth to form an electrode. PtIr/C was used as an anode and PiperION-A20-HCO₃ TP-85 was utilized as the membrane to form a membrane electrode assembly (MEA). Fig. 8a presents the polarisation curve recorded for the corresponding DAFC employing an anode feed consisting of 7 M NH_4OH + 1 M KOH and a cathode feed of CO_2 -free air at different operating temperatures. For comparison, a fuel cell employing a Pt/C cathode was also investigated under similar conditions (Fig. 8b and Fig. 8c).

The effects of operating temperature on fuel cell performance were investigated and are shown in Fig. 8a. The data shows that as temperature increases, there is an obvious increase in overall performance of the DAFC. When temperature was increased from 20 to 40 °C in the DAFC employing LCFCO-700 as a cathode, a notably increase in OCV was observed from 0.3 to 0.6 V. However, as temperature increased above 60 °C, there was minimal change in OCV, with values of 0.69, 0.71 and 0.72 V being obtained at 60, 80 and 100 °C respectively. There is also a substantial increase in current density as operating temperature is increased, with a maximum current density of 379 $mAcm^{-2}$ and peak power density of 34 $mWcm^{-2}$ being obtained at 100 °C. This positive increase in DAFC performance with an increase in operating temperature has commonly been observed in literature [106,107]. Ishiyama et al. reported the effects of temperature on a DAFC employing PGM-based PtRu/C at both the anode and cathode site [107]. At an operating temperature of 50 °C, an OCV and maximum current density of around 0.45 V and 40 $mAcm^{-2}$ was respectively obtained when using 5 M NH_4OH + 1 M KOH as the anodic fuel and air as the cathode stream. A corresponding PPD of 3 $mWcm^{-2}$ was obtained. Under similar operating temperatures of 60 °C, the DAFC shown in Fig. 8b, which utilises similar anodic/cathodic oxidants (7 M NH_4OH + 1 M KOH/air), demonstrates a maximum current density and PPD of 145 $mAcm^{-2}$ and 11

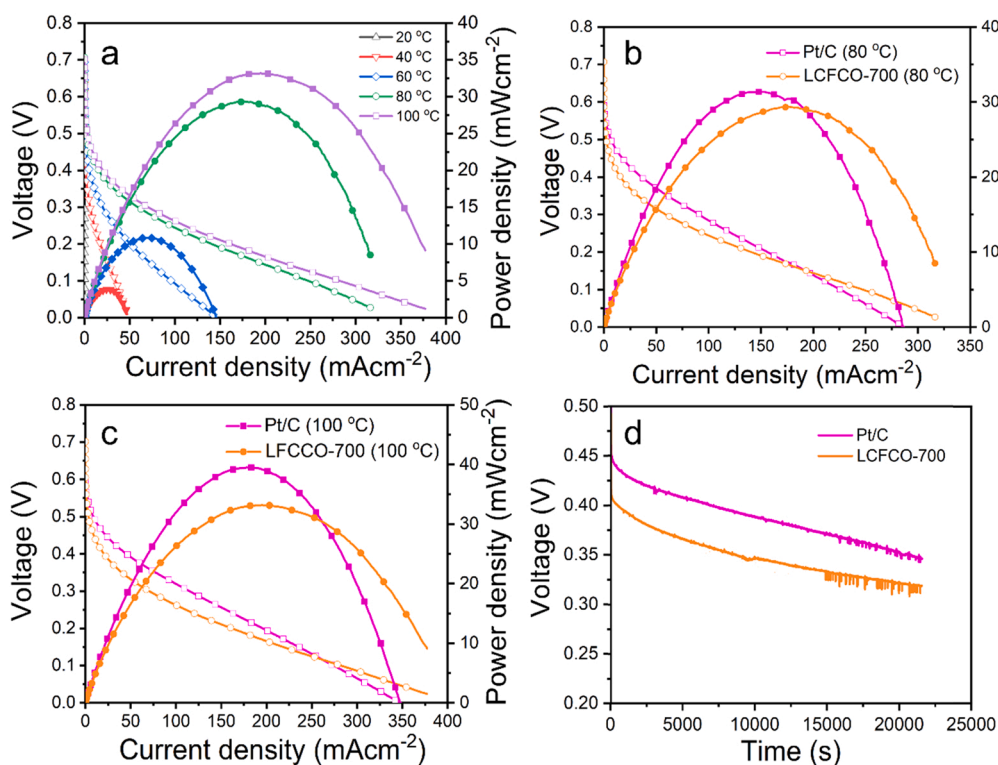


Fig. 8. Polarisation and power density curve of DAFC. (a) Anode: $2.2 \text{ mg}_{\text{PGM}}\text{cm}^{-2}$ PtIr(50 wt%)/C(50 wt %). Cathode: $1.23 \text{ mg}_{\text{oxide}}\text{cm}^{-2}$ LCFCO-700(50 wt%)/C(50 wt %). Test conditions: (1) Anode: 2 mLmin^{-1} of 7 M $\text{NH}_3\text{H}_2\text{O}$ with 1 M KOH; Anode back pressure: 3 bar_g (2) Cathode: 180 mLmin^{-1} CO_2 -free air through humidifier of $T = 95^\circ\text{C}$; Cathode back pressure: 2 bar_g. Cell temperature: 20, 40, 60, 80 and 100°C . (b) Comparison between DAFC employing Pt/C (pink) and LCFCO-700 (orange) cathode at 80°C . (c) Comparison between DAFC employing Pt/C (pink) and LCFCO-700 (orange) cathode at 100°C . For DAFC based on Pt/C cathode - Anode: $2.2 \text{ mg}_{\text{PGM}}\text{cm}^{-2}$ PtIr(50 wt%)/C(50 wt %). Cathode: $0.4 \text{ mg}_{\text{PGM}}\text{cm}^{-2}$ Pt/C. Test conditions: (1) Anode: 2 mLmin^{-1} of 7 M $\text{NH}_3\text{H}_2\text{O}$ with 1 M KOH; Anode back pressure: 3 bar_g (2) Cathode: 180 mLmin^{-1} CO_2 -free air through humidifier of $T = 95^\circ\text{C}$; Cathode back pressure: 2 bar_g. Cell temperature: 80 and 100°C . (d) Stability test of DAFC employing LCFCO-700 and Pt/C-based catalysts at operating temperature of 100°C .

mWcm^{-2} respectively. This reinforces the feasibility of LCFCO-700 to replace PGM-based cathodes in DAFCs, showing their ability to obtain enhanced performances. Furthermore, when the operating temperature was increased in 80°C in the aforementioned study, Ishiyama et al. observed that the OCV and maximum current density increased to around 0.55 V and 48 mAcm^{-2} respectively. A corresponding PPD of 4.5 mWcm^{-2} was obtained for the cell. At the same operating temperature, a maximum current density and PPD of 317 mAcm^{-2} and 30 mWcm^{-2} were respectively obtained in this study. These results illustrate the promising performance of LCFCO-700 as an active and promising cathode under various operating conditions.

Moreover, a closer comparison between Pt/C and LCFCO-700 as cathodes in the DAFC at operating temperatures of 80°C and 100°C are shown in Fig. 8b and Fig. 8c. It should be noted that different loadings were used between the PGM and non-PGM cathodes however, given the high expense of Pt/C as a cathode material, along with the cheap and easy synthesis nature of the LCFCO-700 perovskite, the latter is a promising candidate to replace Pt/C. This would significantly reduce cost of devices such as fuel cells and batteries which rely heavily on PGMs to assist ORR. Nevertheless, the two DAFCs demonstrate very similar performances and power densities and are investigated in further detail below.

The results show an OCV of 0.71 V was achieved when LCFCO was employed as the cathode whereas a lower OCV of 0.60 V was obtained when Pt/C was used. The latter value is common for a DAFC employing Pt/C as a cathode material and is therefore expected [31]. Moreover, a maximum current density of 317 mAcm^{-2} and a peak power density (PPD) of 30 mWcm^{-2} was achieved at an operating temperature of 80°C when LCFCO was employed as the cathode. Remarkably, this performance was very similar to the DAFC employing Pt/C as the cathode, which obtained a maximum current density of 285 mAcm^{-2} and a peak power density of 32 mWcm^{-2} under similar operating conditions. When the temperature was increased to 100°C , an observable enhancement in performance for both fuel cells was observed. Again, the performance was extremely similar, with the DAFC employing LCFCO as the cathode obtaining a maximum current density of 379 mAcm^{-2} and a peak power

density of 34 mWcm^{-2} , and the DAFC employing Pt/C obtaining a maximum current density of 345 mAcm^{-2} and a peak power density of 40 mWcm^{-2} .

Under closer observation, there is a greater potential drop in the low current density regime of the LCFCO-700-based DAFC compared to that of the Pt/C. This region is dominated by the activation overpotential (η_a), which is closely related to: (i) surface conversions preceding the electron transfer such as adsorption on the electrode surface and chemical reactions which are inherent to the catalyst, (ii) electron transfer at the electrode surface of the electrode-electrolyte interface and/or (iii) surface conversions following the electron transfer such as desorption from the electrode surface and chemical reactions which are inherent to the catalyst. Based on these contributing factors, the larger activation overpotential may be due to the surface conversions that occur on Pt compared to LCFCO-700. This is inherent to the catalyst employed and indicates that the Pt surface may facilitate more facile conversion mechanisms and thus lower the activation overpotential associated with the reaction. Furthermore, the electron transfer step plays a key role in this type of overpotential [108]. Since perovskite oxides have inherently lower electrical conductivity than that of platinum, this explanation is plausible and reinforces the need for good electrical contact between the oxide particles [21].

A list of comparative DAFC performances are shown in Table S4. It should be recognised that key studies demonstrated high DAFC performances employ pure O_2 as the oxidant [31,106]. In this study however, CO_2 -free air (20% oxygen) is used as the cathodic oxidant instead of pure O_2 which provides a much safer fuel, particularly for applications such as transport where consumer safety is of upmost importance [1]. Nevertheless, a relatively high current density and high peak power density is still obtained when air is used despite the oxygen content being much lower than pure oxygen. Remarkably, the results in this study are the highest reported for DAFCs employing air as the cathode stream.

Furthermore, the stability of the DAFCs based on LCFCO-700 and Pt/C cathode catalysts were tested in a preliminary durability test at a continuous current density of 50 mA cm^{-2} (Fig. 8d). The results show

that the two cells both demonstrate a steady decrease in voltage over the testing duration and follow the same overall trend, implying comparable nature between the two DAFCs. The fluctuations recorded in the data are owed to ammonia cross over from the anode and cathode, which subsequently lowers voltage over time [1109]. This was visually observed in the outlet of the cathode stream and may partially be owed to employment of a thin polymeric membrane [1].

The results demonstrate that the LCFCO-700 perovskite oxide is an excellent, cheap catalyst for ORR and shows practical applicability in fuel cell devices.

5. Conclusions

A series of $\text{LaCoO}_{3-\delta}$ (LCO) based perovskite oxides including $\text{LaCr}_{0.5}\text{Co}_{0.5}\text{O}_{3-\delta}$ (LCCO), $\text{LaFe}_{0.5}\text{Co}_{0.5}\text{O}_{3-\delta}$ (LFCO) and $\text{LaCr}_{0.25}\text{Fe}_{0.25}\text{Co}_{0.5}\text{O}_{3-\delta}$ (LCFCO) were prepared by a simple sol gel method and their oxygen reduction reaction (ORR) activity was studied in 0.1 M KOH solution at room temperature using a rotating disk electrode (RDE) technique. The highest and lowest ORR activities amongst the electrocatalysts were exhibited by LCFCO and LCO respectively, with the performance of LCFCO being comparable to commercial Pt/C at a much lower cost. The presence of both Cr and Fe were found to play vital roles in enhancing activity, influencing structural and electronic properties respectively. The observed changes in ORR activity of the perovskite electrocatalysts upon doping of Cr was associated with induced changes in the surface oxygen vacancy formation and an increase in the number of transferred electrons to 4, signifying a gradual change in ORR pathway. When introducing Fe into the B-site of the perovskite oxide, a clear enhancement of onset potential E_{onset} was observed in order of $\text{LCFCO} > \text{LFCO} > \text{LCCO} > \text{LCO}$ with values of $0.97 > 0.95 > 0.83 > 0.80$ V vs. RHE respectively. The half-wave potential of LCFCO was also superior (0.86 V vs. RHE) compared to undoped LCO (0.68 V vs. RHE). Furthermore, the effects of calcining temperatures were explored and LCFCO fired at 700 °C (LCFCO-700) was found to give superior activity, with a notable shift in E_{onset} to more positive potentials and the ability to obtain excellent performance at a lower synthesis temperature. Remarkably, when LCFCO-700 was employed in an ammonia-air fuel cell, an OCV of 0.72 V and a maximum current density of $\sim 320 \text{ mAcm}^{-2}$ was achieved, which are comparable to the DAFCs using Pt/C as the cathode, indicating $\text{LaCr}_{0.25}\text{Fe}_{0.25}\text{Co}_{0.5}\text{O}_{3-\delta}/\text{C}$ is a promising non-noble cathode for low temperature fuel cells.

CRedit authorship contribution statement

Georgina Jeerh: Methodology, Investigation, Data curation, Formal analysis, Writing – original draft. **Peimiao Zou:** Data curation. **Mengfei Zhang:** Drawing, plotting. **Shanwen Tao:** Supervision, Conceptualization, Funding acquisition, Writing – review & editing.

Declaration of Competing Interest

The authors declare that they have no known competing financial interests or personal relationships that could have appeared to influence the work reported in this paper.

Data availability

Data will be made available on request.

Acknowledgements

The authors would like to thank EPSRC (Grant No. EP/S515681/1) and Innovate UK (Grant No. 104010 and 133714) for funding. We also thank Dr Marc Walker for collecting and help analysing the XPS data, Dr Ben Breeze for carrying out Raman spectroscopy and Dr Volkan Degirmenci for conducting BET measurements.

Appendix A. Supporting information

Supplementary data associated with this article can be found in the online version at doi:10.1016/j.apcatb.2022.121919.

References

- [1] G. Jeerh, M. Zhang, S. Tao, Recent progress in ammonia fuel cells and their potential applications, *J. Mater. Chem. A* 9 (2021) 727–752.
- [2] H. Zhang, Y. Wang, Z. Wu, D.Y.C. Leung, An ammonia electrolytic cell with NiCu/C as anode catalyst for hydrogen production, *Energy Procedia* 142 (2017) 1539–1544.
- [3] D.J. Little, M.R. Smith III, T.W. Hamann, Electrolysis of liquid ammonia for hydrogen generation, *Energy Environ. Sci.* 8 (2015) 2775–2781.
- [4] F. Vitse, M. Cooper, G.G. Botte, On the use of ammonia electrolysis for hydrogen production, *J. Power Sources* 142 (2005) 18–26.
- [5] B.K. Boggs, G.G. Botte, On-board hydrogen storage and production: an application of ammonia electrolysis, *J. Power Sources* 192 (2009) 573–581.
- [6] S.W. Tao, J.T.S. Irvine, A. Stable, Easily sintered proton-conducting oxide electrolyte for moderate-temperature fuel cells and electrolyzers, *Adv. Mater.* 18 (2006) 1581–1584.
- [7] S. Drespe, F. Luo, R. Schmack, S. Kühl, M. Gliche, P. Strasser, An efficient bifunctional two-component catalyst for oxygen reduction and oxygen evolution in reversible fuel cells, electrolyzers and rechargeable air electrodes, *Energy Environ. Sci.* 9 (2016) 2020–2024.
- [8] S. Park, Y. Shao, J. Liu, Y. Wang, Oxygen electrocatalysts for water electrolyzers and reversible fuel cells: status and perspective, *Energy Environ. Sci.* 5 (2012) 9331–9344.
- [9] M.A. Laguna-Bercero, Recent advances in high temperature electrolysis using solid oxide fuel cells: a review, *J. Power Sources* 203 (2012) 4–16.
- [10] M. Ni, M.K.H. Leung, D.Y.C. Leung, Technological development of hydrogen production by solid oxide electrolyzer cell (SOEC), *Int. J. Hydrog. Energy* 33 (2008) 2337–2354.
- [11] D. Banham, S. Ye, Current status and future development of catalyst materials and catalyst layers for proton exchange membrane fuel cells: an industrial perspective, *ACS Energy Lett.* 2 (2017) 629–638.
- [12] M. Zhang, G. Jeerh, P. Zou, R. Lan, M. Wang, H. Wang, S.W. Tao, Recent development of perovskite oxide-based electrocatalysts and their applications in low to intermediate temperature electrochemical devices, *Mater. Today* 49 (2021) 351–377.
- [13] J. Irvine, J. Rupp, G. Liu, X. Xu, S.M. Haile, X. Qian, A. Snyder, R. Freer, D. Eken, S. Skinner, O. Celikbilek, S. Chen, S.W. Tao, T.H. Shin, R. O'Hayre, J. Huang, C. Duan, M. Papac, S. Li, A. Russel, V. Celorrio, B. Hayden, H. Nolan, X. Huang, G. Wang, I. Metcalfe, D. Neagu, S.G. Martin, Roadmap on inorganic perovskites for energy applications, *J. Phys.: Energy* 3 (2021), 031502.
- [14] P.I. Cowin, C.T.G. Petit, R. Lan, J.T.S. Irvine, S.W. Tao, Recent progress in the development of anode materials for solid oxide fuel cells, *Adv. Energy Mater.* 1 (2011) 314–332.
- [15] M. Zhang, H. Li, X. Duan, P. Zou, G. Jeerh, B. Sun, S. Chen, J. Humphreys, M. Walker, K. Xie, S.W. Tao, An efficient symmetric electrolyzer based on bifunctional perovskite catalyst for ammonia electrolysis, *Adv. Sci.* 8 (2021) 210299.
- [16] B. Lin, M. Hu, J. Ma, Y. Jiang, S.W. Tao, G. Meng, Stable, easily sintered $\text{BaCe}_{0.5}\text{Zr}_{0.3}\text{Y}_{0.16}\text{Zn}_{0.04}\text{O}_{3-\delta}$ electrolyte-based protonic ceramic membrane fuel cells with $\text{Ba}_{0.5}\text{Sr}_{0.5}\text{Zn}_{0.2}\text{Fe}_{0.8}\text{O}_{3-\delta}$ perovskite cathode, *J. Power Sources* 183 (2008) 479–484.
- [17] X. Xu, H. Sun, S.P. Jiang, Z. Shao, Modulating metal–organic frameworks for catalyzing acidic oxygen evolution for proton exchange membrane water electrolysis, *SusMat* 1 (2021) 460–481.
- [18] L. Shen, M. Ma, F. Tu, Z. Zhao, Y. Xia, K. Goh, L. Zhao, Z. Wang, G. Shao, Recent advances in high-loading catalysts for low-temperature fuel cells: from nanoparticle to single atom, *SusMat* 1 (2021) 569–592.
- [19] W. Xu, Z.C. Wu, S.W. Tao, Recent progress in electrocatalysts with mesoporous structures for application in polymer electrolyte membrane fuel cells, *J. Mater. Chem. A* 4 (2016) 16272–16287.
- [20] X. Ge, A. Sumboja, D. Wu, T. An, B. Li, F.W.T. Goh, T.S.A. Hor, Y. Zong, Z. Liu, Oxygen reduction in alkaline media: from mechanisms to recent advances of catalysts, *ACS Catal.* 5 (2015) 4643–4667.
- [21] Y. Zhu, W. Zhou, Z. Shao, Perovskite/carbon composites: applications in oxygen electrocatalysis, *Small* 13 (2017) 1603793.
- [22] A. Brouzgou, S. Song, Z.-X. Liang, P. Tsiakaras, Non-precious electrocatalysts for oxygen reduction reaction in alkaline media: latest achievements on novel carbon materials, *Catalysts* 6 (2016) 159.
- [23] J. Suntivich, H.A. Gasteiger, N. Yabuuchi, H. Nakanishi, J.B. Goodenough, Y. Shao-Horn, Design principles for oxygen-reduction activity on perovskite oxide catalysts for fuel cells and metal–air batteries, *Nat. Chem.* 3 (2011) 546–550.
- [24] W.T. Hong, M. Risch, K.A. Stoerzinger, A. Grimaud, J. Suntivich, Y. Shao-Horn, Toward the rational design of non-precious transition metal oxides for oxygen electrocatalysis, *Energy Environ. Sci.* 8 (2015) 1404–1427.
- [25] P. Zou, S. Chen, R. Lan, J. Humphreys, G. Jeerh, S. Tao, Investigation of perovskite oxide $\text{SrFe}_{0.8}\text{Cu}_{0.1}\text{Nb}_{0.1}\text{O}_{3-\delta}$ as cathode for a room temperature direct ammonia fuel cell, *Int. J. Hydrog. Energy* 44 (2019) 26554–26564.

- [26] P. Zou, S. Chen, R. Lan, S. Tao, Investigation of perovskite oxide $\text{SrCo}_{0.8}\text{Cu}_{0.1}\text{Nb}_{0.1}\text{O}_{3-\delta}$ as a cathode material for room temperature direct ammonia fuel cells, *ChemSusChem* 12 (2019) 2788–2794.
- [27] J. Greeley, I.E.L. Stephens, A.S. Bondarenko, T.P. Johansson, H.A. Hansen, T. F. Jaramillo, J. Rossmeisl, I. Chorkendorff, J.K. Nørskov, Alloys of platinum and early transition metals as oxygen reduction electrocatalysts, *Nat. Chem.* 1 (2009) 552–556.
- [28] V.R. Stamenkovic, B. Fowler, B.S. Mun, G. Wang, P.N. Ross, C.A. Lucas, N. M. Marković, Improved oxygen reduction activity on $\text{Pt}_3\text{Ni}(111)$ via increased surface site availability, *Science* 315 (2007) 493–497.
- [29] M. Retuerto, A.G. Pereira, F.J. Pérez-Alonso, M.A. Peña, J.L.G. Fierro, J.A. Alonso, M.T. Fernández-Díaz, L. Pascual, S. Rojas, Structural effects of LaNiO_3 as electrocatalyst for the oxygen reduction reaction, *Appl. Catal. B: Environ.* 203 (2017) 363–371.
- [30] X. Yang, C. Priest, Y. Hou, G. Wu, Atomically dispersed dual-metal-site PGM-free electrocatalysts for oxygen reduction reaction: Opportunities and challenges, *SusMat* (2022), <https://doi.org/10.1002/sus1002.1069>.
- [31] Y. Zhao, B.P. Setzler, J. Wang, J. Nash, T. Wang, B. Xu, Y. Yan, An efficient direct ammonia fuel cell for affordable carbon-neutral transportation, *Joule* 3 (2019) 2472–2484.
- [32] R. Lan, S. Tao, Ammonia as a suitable fuel for fuel cells, *Front. Energy Res.* 2 (2014) 35.
- [33] C. Smith, A.K. Hill, L. Torrente-Murciano, Current and future role of Haber–Bosch ammonia in a carbon-free energy landscape, *Energy Environ. Sci.* 13 (2020) 331–344.
- [34] J. Hansson, S. Brynolf, E. Fridell, M. Lehtveer, The potential role of ammonia as marine fuel—based on energy systems modeling and multi-criteria decision analysis, *Sustainability* 12 (2020) 3265.
- [35] Z. Cesaro, M. Ives, R. Nayak-Luke, M. Mason, R. Bañares-Alcántara, Ammonia to power: forecasting the levelized cost of electricity from green ammonia in large-scale power plants, *Appl. Energy* 282 (2021), 116009.
- [36] D.R. MacFarlane, P.V. Cherepanov, J. Choi, B.H.R. Suryanto, R.Y. Hodgetts, J. M. Bakker, F.M. Ferrero Vallana, A.N. Simonov, A roadmap to the ammonia economy, *Joule* 4 (2020) 1186–1205.
- [37] R. Lan, S.W. Tao, Direct ammonia alkaline anion-exchange membrane fuel cells, *Electrochem. Solid-State Lett.* 13 (2010) B83–B86.
- [38] Y. Li, H.S. Pillai, T. Wang, S. Hwang, Y. Zhao, Z. Qiao, Q. Mu, S. Karakalos, M. Chen, J. Yang, High-performance ammonia oxidation catalysts for anion-exchange membrane direct ammonia fuel cells, *Energy Environ. Sci.* 14 (2021) 1449–1460.
- [39] M.F. Zhang, P.M. Zou, G. Jeerh, S.G. Chen, J. Shields, H.T. Wang, S.W. Tao, Electricity generation from ammonia in landfill leachate by an alkaline membrane fuel cell based on precious-metal-free electrodes, *ACS Sustain. Chem. Eng.* 8 (2020) 12817–12824.
- [40] G. Jeerh, P. Zou, M. Zhang, S. Chen, J. Humphreys, S.W. Tao, Electrooxidation of ammonia on A-site deficient perovskite oxide $\text{La}_{0.9}\text{Ni}_{0.6}\text{Cu}_{0.35}\text{Fe}_{0.05}\text{O}_{3-\delta}$ for wastewater treatment, *Sep. Purif. Technol.* 297 (2022), 121451.
- [41] M. Zhang, P. Zou, G. Jeerh, B. Sun, M. Walker, S.W. Tao, Oxygen vacancy-rich $\text{La}_{0.5}\text{Sr}_{1.5}\text{Ni}_{0.4}\text{Cu}_{0.1}\text{O}_{4-\delta}$ as a high-performance bifunctional catalyst for symmetric ammonia electrolyzer, *Adv. Funct. Mater.* n/a (2022) 2204881.
- [42] A. Safakas, G. Bampos, S. Bebelis, Oxygen reduction reaction on $\text{La}_{0.8}\text{Sr}_{0.2}\text{CoFe}_{1-x}\text{O}_{3-\delta}$ perovskite/carbon black electrocatalysts in alkaline medium, *Appl. Catal. B: Environ.* 244 (2019) 225–232.
- [43] J. Liu, L. Jiang, B. Zhang, J. Jin, D.S. Su, S. Wang, G. Sun, Controllable synthesis of cobalt monoxide nanoparticles and the size-dependent activity for oxygen reduction reaction, *ACS Catal.* 4 (2014) 2998–3001.
- [44] J. Hwang, R.R. Rao, L. Giordano, Y. Katayama, Y. Yu, Y. Shao-Horn, Perovskites in catalysis and electrocatalysis, *Science* 358 (2017) 751–756.
- [45] M. Zhang, G. Jeerh, P. Zou, R. Lan, M. Wang, H. Wang, S. Tao, Recent development of perovskite-based electrocatalysts and their applications in low to intermediate temperature electrochemical devices, *Mater. Today* (2021).
- [46] M. Yasumiti, Y. Hiroshi, T. Hideo, A new catalyst for cathodic reduction of oxygen: lanthanum nickel oxide, *Chem. Lett.* 4 (1975) 661–662.
- [47] J. Sunarso, A.A.J. Torriero, W. Zhou, P.C. Howlett, M. Forsyth, Oxygen reduction reaction activity of la-based perovskite oxides in alkaline medium: a thin-film rotating ring-disk electrode study, *J. Phys. Chem. C* 116 (2012) 5827–5834.
- [48] J. Sun, L. Du, B. Sun, G. Han, Y. Ma, J. Wang, H. Huo, C. Du, G. Yin, Bifunctional $\text{LaMn}_{0.3}\text{Co}_{0.7}\text{O}_3$ perovskite oxide catalyst for oxygen reduction and evolution reactions: the optimized eg electronic structures by manganese dopant, *ACS Appl. Mater. Interfaces* 12 (2020) 24717–24725.
- [49] Z. Wang, Y. You, J. Yuan, Y.-X. Yin, Y.-T. Li, S. Xin, D. Zhang, Nickel-doped $\text{La}_{0.8}\text{Sr}_{0.2}\text{Mn}_{1-x}\text{Ni}_x\text{O}_3$ nanoparticles containing abundant oxygen vacancies as an optimized bifunctional catalyst for oxygen cathode in rechargeable lithium–air batteries, *ACS Appl. Mater. Interfaces* 8 (2016) 6520–6528.
- [50] M. Risch, Perovskite electrocatalysts for the oxygen reduction reaction in alkaline media, *Catalysts* 7 (2017) 154.
- [51] C. Sun, J.A. Alonso, J. Bian, Recent advances in perovskite-type oxides for energy conversion and storage applications, *Adv. Energy Mater.* 11 (2021) 2000459.
- [52] M.A. Peña, J.L.G. Fierro, Chemical structures and performance of perovskite oxides, *Chem. Rev.* 101 (2001) 1981–2018.
- [53] R.A. Van Santen, M. Neurock, Concepts in theoretical heterogeneous catalytic reactivity, *Catal. Rev.* 37 (1995) 557–698.
- [54] Y. Matsumoto, H. Yoneyama, H. Tamura, Catalytic activity for electrochemical reduction of oxygen of lanthanum nickel oxide and related oxides, *J. Electroanal. Chem. Interfacial Electrochem.* 79 (1977) 319–326.
- [55] Y. Matsumoto, H. Yoneyama, H. Tamura, Influence of the nature of the conduction band of transition metal oxides on catalytic activity for oxygen reduction, *J. Electroanal. Chem. Interfacial Electrochem.* 83 (1977) 237–243.
- [56] B. Hammer, Special sites at noble and late transition metal catalysts, *Top. Catal.* 37 (2006) 3–16.
- [57] J. Suntivich, K.J. May, H.A. Gasteiger, J.B. Goodenough, Y. Shao-Horn, A. Perovskite, Oxide optimized for oxygen evolution catalysis from molecular orbital principles, *Science* 334 (2011) 1383.
- [58] J.O.M. Bockris, T. Otagawa, The electrocatalysis of oxygen evolution on perovskites, *J. Electrochem. Soc.* 131 (1984) 290–302.
- [59] X. Xu, Y. Pan, W. Zhou, Y. Chen, Z. Zhang, Z. Shao, Toward enhanced oxygen evolution on perovskite oxides synthesized from different approaches: a case study of $\text{Ba}_{0.5}\text{Sr}_{0.5}\text{Co}_{0.8}\text{Fe}_{0.2}\text{O}_{3-\delta}$, *Electrochim. Acta* 219 (2016) 553–559.
- [60] W.T. Hong, R.E. Welsch, Y. Shao-Horn, Descriptors of oxygen-evolution activity for oxides: a statistical evaluation, *J. Phys. Chem. C* 120 (2016) 78–86.
- [61] M.P. Pechini, USA Patent, 3,330,697 (1967).
- [62] T. Poux, F.S. Napolskiy, T. Dintzer, G. Kéranguéven, S.Y. Istomin, G.A. Tsirlina, E. V. Antipov, E.R. Savinova, Dual role of carbon in the catalytic layers of perovskite/carbon composites for the electrocatalytic oxygen reduction reaction, *Catal. Today* 189 (2012) 83–92.
- [63] M. Jahan, Q. Bao, K.P. Loh, Electrocatalytically active graphene–porphyrin mof composite for oxygen reduction reaction, *J. Am. Chem. Soc.* 134 (2012) 6707–6713.
- [64] M.H.M.T. Assumpção, S.G. da Silva, R.F.B. de Souza, G.S. Buzzo, E.V. Spinacé, A. O. Neto, J.C.M. Silva, Direct ammonia fuel cell performance using PtIr/C as anode electrocatalysts, *Int. J. Hydrog. Energy* 39 (2014) 5148–5152.
- [65] S. Ajmal, I. Bibi, F. Majid, S. Ata, K. Kamran, K. Jilani, S. Nouren, S. Kamal, A. Ali, M. Iqbal, Effect of Fe and Bi doping on LaCoO_3 structural, magnetic, electric and catalytic properties, *J. Mater. Res. Technol.* 8 (2019) 4831–4842.
- [66] A. Ishikawa, J. Nohara, S. Sugai, Raman Study of the Orbital-Phonon Coupling in LaCoO_3 , *Phys. Rev. Lett.* 93 (2004), 136401.
- [67] A. Gholizadeh, The effects of A/B-site substitution on structural, redox and catalytic properties of lanthanum ferrite nanoparticles, *J. Mater. Res. Technol.* 8 (2019) 457–466.
- [68] N.A. Merino, B.P. Barbero, P. Ruiz, L.E. Cadús, Synthesis, characterisation, catalytic activity and structural stability of $\text{LaCo}_{1-y}\text{Fe}_y\text{O}_{3\pm\lambda}$ perovskite catalysts for combustion of ethanol and propane, *J. Catal.* 240 (2006) 245–257.
- [69] R. Shannon, Revised effective ionic radii and systematic studies of interatomic distances in halides and chalcogenides, *Acta Crystallogr. Sect. A* 32 (1976) 751–767.
- [70] S. Ivanova, A. Senyshyn, E. Zhecheva, K. Tenchev, R. Stoyanova, H. Fuess, Crystal structure, microstructure and reducibility of $\text{LaNiCo}_{1-x}\text{O}_3$ and $\text{LaFeCo}_{1-x}\text{O}_3$ Perovskites ($0 < x \leq 0.5$), *J. Solid State Chem.* 183 (2010) 940–950.
- [71] A.C. Larson, R.B.V. Dreele, General structure analysis system (GSAS) (Los Alamos National Laboratory Report), The Reagents of the University of California, 2004.
- [72] B.H. Toby, EXPGUI, a graphical user interface for GSAS, *J. Appl. Crystallogr.* 34 (2001) 210–213.
- [73] M. Popa, L.V. Hong, M. Kakihana, Nanopowders of LaMeO_3 perovskites obtained by a solution-based ceramic processing technique, *Phys. B: Condens. Matter* 327 (2003) 233–236.
- [74] W.T. Hong, M. Gadre, Y.-L. Lee, M.D. Biegalski, H.M. Christen, D. Morgan, Y. Shao-Horn, Tuning the Spin State in LaCoO_3 Thin Films for Enhanced High-Temperature Oxygen Electrocatalysis, *J. Phys. Chem. Lett.* 4 (2013) 2493–2499.
- [75] M.F. Sunding, K. Hadidi, S. Diplax, O.M. Løvvik, T.E. Norby, A.E. Gunnæs, XPS characterisation of in situ treated lanthanum oxide and hydroxide using tailored charge referencing and peak fitting procedures, *J. Electron Spectrosc. Relat. Phenom.* 184 (2011) 399–409.
- [76] M.C. Biesinger, B.P. Payne, A.P. Grosvenor, L.W.M. Lau, A.R. Gerson, R.S. C. Smart, Resolving surface chemical states in XPS analysis of first row transition metals, oxides and hydroxides: Cr, Mn, Fe, Co and Ni, *Appl. Surf. Sci.* 257 (2011) 2717–2730.
- [77] X. Wang, X. Peng, H. Ran, B. Lin, J. Ni, J. Lin, L. Jiang, Influence of Ru Substitution on the Properties of LaCoO_3 Catalysts for Ammonia Synthesis: XAFS and XPS Studies, *Ind. Eng. Chem. Res.* 57 (2018) 17375–17383.
- [78] Y. Liu, H. Dai, J. Deng, S. Xie, H. Yang, W. Tan, W. Han, Y. Jiang, G. Guo, Mesoporous Co_3O_4 -supported gold nanoparticles: Highly active for the oxidation of carbon monoxide, benzene, toluene, and o-xylene, *J. Catal.* 309 (2014) 408–418.
- [79] L.F. Liotta, G. Di Carlo, G. Pantaleo, A.M. Venezia, G. Deganello, $\text{Co}_3\text{O}_4/\text{CeO}_2$ composite oxides for methane emissions abatement: Relationship between Co_3O_4 – CeO_2 interaction and catalytic activity, *Appl. Catal. B: Environ.* 66 (2006) 217–227.
- [80] Y. Lu, A. Ma, Y. Yu, R. Tan, C. Liu, P. Zhang, D. Liu, J. Gui, Engineering oxygen vacancies into LaCoO_3 perovskite for efficient electrocatalytic oxygen evolution, *ACS Sustain. Chem. Eng.* 7 (2019) 2906–2910.
- [81] X. Gao, Z. Sun, J. Ran, J. Li, J. Zhang, D. Gao, High efficiency electrocatalyst of $\text{LaCr}_{0.5}\text{Fe}_{0.5}\text{O}_3$ nanoparticles on oxygen-evolution reaction, *Sci. Rep.* 10 (2020) 13395.
- [82] Y. Zhu, W. Zhou, J. Yu, Y. Chen, M. Liu, Z. Shao, Enhancing electrocatalytic activity of perovskite oxides by tuning cation deficiency for oxygen reduction and evolution reactions, *Chem. Mater.* 28 (2016) 1691–1697.
- [83] J. Suntivich, H.A. Gasteiger, N. Yabuuchi, Y. Shao-Horn, Electrocatalytic measurement methodology of oxide catalysts using a thin-film rotating disk electrode, *J. Electrochem. Soc.* 157 (2010) B1263.
- [84] T.-N. Tran, M.Y. Song, K.P. Singh, D.-S. Yang, J.-S. Yu, Iron–polypyrrole electrocatalyst with remarkable activity and stability for ORR in both alkaline and

- acidic conditions: a comprehensive assessment of catalyst preparation sequence, *J. Mater. Chem. A* 4 (2016) 8645–8657.
- [85] T.-W. Chen, P. Kalimuthu, G. Anushya, S.-M. Chen, R. Ramachandran, V. Mariyappan, D.C. Muthumala, High-efficiency of Bi-functional-based perovskite nanocomposite for oxygen evolution and oxygen reduction reaction: an overview, *Mater. (Basel)* 14 (2021) 2976.
- [86] D.E. Beltrán, S. Litster, Half-wave potential or mass activity? Characterizing platinum group metal-free fuel cell catalysts by rotating disk electrodes, *ACS Energy Lett.* 4 (2019) 1158–1161.
- [87] F. Jaouen, J. Herranz, M. Lefèvre, J.-P. Dodelet, U.I. Kramm, I. Herrmann, P. Bogdanoff, J. Maruyama, T. Nagaoka, A. Garsuch, J.R. Dahn, T. Olson, S. Pylypenko, P. Atanassov, E.A. Ustinov, Cross-laboratory experimental study of non-noble-metal electrocatalysts for the oxygen reduction reaction, *Appl. Mater. Interfaces* 1 (2009) 1623–1639.
- [88] A. Serov, M.H. Robson, K. Artyushkova, P. Atanassov, Templated non-PGM cathode catalysts derived from iron and poly(ethyleneimine) precursors, *Appl. Catal. B: Environ.* 127 (2012) 300–306.
- [89] A. Serov, K. Artyushkova, P. Atanassov, Fe-N-C oxygen reduction fuel cell catalyst derived from carbendazim: synthesis, structure, and reactivity, *Advanced Energy Materials* 4 (2014) 1301735.
- [90] X. Li, G. Liu, B.N. Popov, Activity and stability of non-precious metal catalysts for oxygen reduction in acid and alkaline electrolytes, *J. Power Sources* 195 (2010) 6373–6378.
- [91] W. Xia, J. Zhu, W. Guo, L. An, D. Xia, R. Zou, Well-defined carbon polyhedrons prepared from nano metal–organic frameworks for oxygen reduction, *J. Mater. Chem. A* 2 (2014) 11606–11613.
- [92] R.-h Yuan, Y. He, W. He, M. Ni, M.K.H. Leung, Bifunctional electrocatalytic activity of $\text{La}_{0.8}\text{Sr}_{0.2}\text{MnO}_3$ -based perovskite with the A-site deficiency for oxygen reduction and evolution reactions in alkaline media, *Appl. Energy* 251 (2019), 113406.
- [93] Q. Ji, L. Bi, J. Zhang, H. Cao, X.S. Zhao, The role of oxygen vacancies of ABO_3 perovskite oxides in the oxygen reduction reaction, *Energy Environ. Sci.* 13 (2020) 1408–1428.
- [94] C. Jin, X. Cao, F. Lu, Z. Yang, R. Yang, Electrochemical study of $\text{Ba}_{0.5}\text{Sr}_{0.5}\text{Co}_{0.8}\text{Fe}_{0.2}\text{O}_3$ perovskite as bifunctional catalyst in alkaline media, *Int. J. Hydrog. Energy* 38 (2013) 10389–10393.
- [95] F. Lu, J. Sui, J. Su, C. Jin, M. Shen, R. Yang, Hollow spherical $\text{La}_{0.8}\text{Sr}_{0.2}\text{MnO}_3$ perovskite oxide with enhanced catalytic activities for the oxygen reduction reaction, *J. Power Sources* 271 (2014) 55–59.
- [96] E. García-López, G. Marci, F. Puleo, V. La Parola, L.F. Liotta, $\text{La}_{1-x}\text{Sr}_x\text{Co}_{1-y}\text{Fe}_y\text{O}_{3-\delta}$ perovskites: preparation, characterization and solar photocatalytic activity, *Appl. Catal. B: Environ.* 178 (2015) 218–225.
- [97] R.S. Kalubarme, G.-E. Park, K.-N. Jung, K.-H. Shin, W.-H. Ryu, C.-J. Park, $\text{LaNi}_x\text{Co}_{1-x}\text{O}_{3-\delta}$ perovskites as catalyst material for non-aqueous lithium-oxygen batteries, *J. Electrochem. Soc.* 161 (2014) A880–A889.
- [98] Z. Du, P. Yang, L. Wang, Y. Lu, J.B. Goodenough, J. Zhang, D. Zhang, Electrocatalytic performances of $\text{LaNi}_{1-x}\text{Mg}_x\text{O}_3$ perovskite oxides as bi-functional catalysts for lithium air batteries, *J. Power Sources* 265 (2014) 91–96.
- [99] D. Zhang, Y. Song, Z. Du, L. Wang, Y. Li, J.B. Goodenough, Active $\text{LaNi}_{1-x}\text{Fe}_x\text{O}_3$ bifunctional catalysts for air cathodes in alkaline media, *J. Mater. Chem. A* 3 (2015) 9421–9426.
- [100] R. Schmidt, J. Wu, C. Leighton, I. Terry, Dielectric response to the low-temperature magnetic defect structure and spin state transition in polycrystalline LaCoO_3 , *Phys. Rev. B* 79 (2009), 125105.
- [101] M.A. Korotin, S.Y. Ezhov, I.V. Solov'ev, V.I. Anisimov, D.I. Khomskii, G. A. Sawatzky, Intermediate-spin state and properties of LaCoO_3 , *Phys. Rev. B* 54 (1996) 5309–5316.
- [102] A. Tsuruta, S. Kawasaki, M. Mikami, Y. Kinemuchi, Y. Masuda, A. Fujita, I. Terasaki, Co-substitution effect in room-temperature ferromagnetic oxide $\text{Sr}_{3.1}\text{Y}_{0.9}\text{Co}_4\text{O}_{10.5}$, *Materials* 13 (2020).
- [103] A.M. Durand, D.P. Belanger, C.H. Booth, F. Ye, S. Chi, J.A. Fernandez-Baca, M. Bhat, Magnetism and phase transitions in LaCoO_3 , *J. Phys.: Condens. Matter* 25 (2013), 382203.
- [104] C.S. Naiman, R. Gilmore, B. DiBartolo, A. Linz, R. Santoro, Interpretation of the magnetic properties of LaCoO_3 , *J. Appl. Phys.* 36 (1965) 1044–1045.
- [105] T. Wang, Y. Zhao, B.P. Setzler, R. Abbasi, S. Gottesfeld, Y. Yan, A. High-Performance, 75 W direct ammonia fuel cells stack, *Energy* (2021).
- [106] B. Achrai, Y. Zhao, T. Wang, G. Tamir, R. Abbasi, B.P. Setzler, M. Page, Y. Yan, S. Gottesfeld, A direct ammonia fuel cell with a KOH-free anode feed generating 180 mW cm^{-2} at 120 °C, *J. Electrochem. Soc.* 167 (2020), 134518.
- [107] S. Ishiyama, N.C. Rosero-Navarro, A. Miura, K. Tadanaga, Mg-Al layered double hydroxide as an electrolyte membrane for aqueous ammonia fuel cell, *Mater. Res. Bull.* 119 (2019), 110561.
- [108] W. Wang, X. Wei, D. Choi, X. Lu, G. Yang, C. Sun, Chapter 1 - Electrochemical cells for medium- and large-scale energy storage: fundamentals, in: C. Menictas, M. Skyllas-Kazacos, T.M. Lim (Eds.), *Advances in Batteries for Medium and Large-Scale Energy Storage*, Woodhead Publishing, 2015, pp. 3–28.
- [109] S. Suzuki, H. Muroyama, T. Matsui, K. Eguchi, Fundamental studies on direct ammonia fuel cell employing anion exchange membrane, *J. Power Sources* 208 (2012) 257–262.